Exploring Links between Climate and Orogeny by Estimating Uplift with a Physical-Statistical Model

by

Lauren E. L. Lowman

Department of Civil and Environmental Engineering
Duke University

Date: _____

Approved:

_____
Ana P. Barros, Supervisor

_____
Marco Marani

_____
Wenhong Li

Thesis submitted in partial fulfillment of the requirements for the degree of
Master of Science in the Department of Civil and Environmental Engineering
in the Graduate School of Duke University
2013

Abstract

Exploring Links between Climate and Orogeny by Estimating Uplift with a Physical-Statistical Model

by

Lauren E. L. Lowman

Department of Civil and Environmental Engineering
Duke University

Date: _____

Approved:

_____
Ana P. Barros, Supervisor

_____
Marco Marani

_____
Wenhong Li

An abstract of a thesis submitted in partial fulfillment of the requirements for the degree of Master of Science in the Department of Civil and Environmental Engineering
in the Graduate School of Duke University
2013

Abstract

The Andes Mountains provide a unique setting to study the interplay between climate and geomorphology. The mechanism proposed to describe the evolution of Andean topography is a feedback loop where precipitation erodes the surface, causing the earth's crust to thin and, through buoyancy, uplift the surface. The uplifted surface acts as a barrier which in turn increases precipitation and reinforces the feedback. Demonstrating this feedback is difficult due to the long temporal scales involved. To overcome this challenge, we consider current topographic constraints and climate regimes as a means to evaluate geomorphologic behavior. Initial data analysis leads to the identification of qualitative similarities in the distributions of outlets and precipitation events by elevation, which suggest a link between climatic and fluvial erosion and a strong interaction between orography and precipitation. To explore impacts of this link on regional geomorphology, we estimate uplift rates under a Bayesian hierarchical modeling framework based on the stream power erosion law (SPEL). We specify model parameters using slope and area data generated from a high-resolution, digital elevation map and mean annual precipitation (MAP) derived from 14 years of TRMM 3B42 v.7 precipitation rainfall rates, supplemented with rain gauge data from the Kospiñata network in Peru. A key component of the analysis is the development of a natural spatial scale which captures the qualitative similarities observed in the region and provides a means to compare estimated uplift rates to the geomorphologic behavior of each basin. The estimated uplift values recovered

from the analysis range from 0.81 to 11.59 mm/yr and thus fall within a physically-reasonable range for the central Andes region. These estimates also are in strong agreement with basin hypsometry. The analysis further reveals a pattern of spatially dependent uplift, which is consistent with the differential tectonic forcing imposed on the basins by the subducting Nazca plate. The adaptation of the physical-statistical model represents a novel method for quantifying the relationship between climate and orography and estimating key parameters of SPEL.

This work is dedicated to my loving husband Nick who has pushed me to do more than I ever imagined I could.

Contents

List of Tables

List of Figures

Acknowledgements

Thank you first and foremost to my adviser Professor Ana Barros who has guided and encouraged me through this entire process. I am forever grateful for the opportunities to grow and learn that have been afforded to me under your mentorship. I would also like to thank my committee members Professors Marco Marani and Wenhong Li for their participation and valuable feedback. Thank you to Professor Chuntao Liu and his group at the University of Utah for providing the TRMM PF data analyzed in the study. Finally, I want to acknowledge the Pratt School of Engineering for its support as I pursued graduate studies at Duke University.

1

Introduction

1.1 Statement of Problem

Establishing and quantifying a relationship between climate and orogenic deformation is of fundamental importance to our understanding of earth system interactions and has garnered interdisciplinary interest from geologists and climatologists. While it is accepted and understood that precipitation is paramount to erosional processes in mountainous regions, the question lies in how to demonstrate the existence of a feedback loop between precipitation, erosion, and tectonic activity. It has been proposed that the basic feedback is simply Archimedes' principle in which mechanical erosion of the surface due to precipitation results in localized thinning of the crust and thus spatially dependent uplift patterns (Hodges, 2006). However, the long geologic timescales over which these processes occur create difficulty in demonstrating such an effect.

Due to the strong presence of orographic precipitation in the region, a number of studies evaluate the proposed feedback in the Andes Mountains (e.g., Hoorn et al., 2010; Strecker et al., 2009; McQuarrie et al., 2008; Strecker et al., 2007; Hilley et al.,

2004; Montgomery et al., 2001). Hoorn et al. (2010) discusses the large, regional effect uplift in the Andes has had on climate, landscape, and wildlife on the South American continent, and particularly in the Amazon basin. They state that a coupling of climate and tectonics led to further uplift of the Andes Mountains and argue that sediment fluxes from higher elevations to lower elevations allowed for the creation of species-specific habitats. Montgomery et al. (2001) suggest that the regional hypsometry of the Andes mountain chain demonstrate the role of climate in orogenic erosion. Aalto et al. (2006) find basin area, lithology, and average slope to be statistically significant controls of average annual basin sediment flux. In the central Andes region, much attention has been paid to the role of the Puña Plateau in orogenic development and climate change. Strecker et al. (2007) find that a link between precipitation, erosion, and tectonics allowed for the development of the Puña Plateau in the central-southern Andes which in turn modified precipitation patterns and allows for a more humid climate along the eastern side of the orogen. This finding agrees with Strecker et al. (2009) who find that a delicate balance must exist between climate-controlled erosion and tectonic uplift to maintain the landscape of the plateau. McQuarrie et al. (2008) conclude that changes in precipitation patterns over time between the northern and southern Andes may be related to the rise of the Puña Plateau that surpassed a critical height and led to the strengthening of precipitation in the Bolivian Andes. While the studies described here provide compelling evidence of a feedback loop, they lack a quantitative demonstration of its existence. Here we propose to evaluate the interplay of climate and tectonics in the central Andes through a physically-based statistical model.

A common tool for investigating linkages between climate and tectonics is the stream power erosion law (SPEL). SPEL was derived from a basic postulate that the erosion rate is proportional to shear stress and is easily manipulated to account for different erosion and incision processes that span a wide range of geologic areas

(e.g., Whipple and Tucker, 1999; Whipple and Meade, 2004). It has been extensively demonstrated that, when parameterized correctly, this simple mathematical model captures actual orogenic structure and erodibility behavior (e.g., Hilley and Strecker, 2004; Hilley et al., 2004; Willett, 1999). The flexibility of this model has allowed for the direct incorporation of orographically-enhanced precipitation effects on the evolution of river profiles. The inclusion of this effect has a significant impact on steady-state channel profiles, the magnitude of which is strongly dependent on precipitation regimes and climatology (Wu et al., 2006; Roe et al., 2003, 2002).

Thus, the effectiveness of the SPEL model in capturing the essential physics of orogenic evolution has been shown under the correct parameterizations. The key physical parameters are often assumed, as it is difficult, if at all possible, to measure these directly. Under steady-state assumptions, a constraint on the SPEL parameters may be determined through the slope-area analysis technique developed by Snyder et al. (2000) which involves determining two unknowns in one equation; however, in mountainous regions where the orographic precipitation effect is strong, the simplification that allows for this no longer holds since there are more unknowns to consider (Finlayson and Montgomery, 2003; Roe et al., 2002). Choice of these parameters has been shown to influence orogen response to climate and tectonic forcings in numerical simulations (Hilley et al., 2004; Hilley and Strecker, 2004; Roe et al., 2003; Tucker and Whipple, 2002; Whipple and Tucker, 1999). Here, we demonstrate a methodology to estimate the key physical parameters of SPEL within a Bayesian hierarchical framework. We focus specifically on the uplift parameter which can readily be compared to measured values found in previous literature.

The standard means of estimating uplift rates are geologically-informed inferences based on evidence from fission-track dating, clumped isotopes, and paleosurface reconstruction. The difficulty with the application and interpretation of these methods is that they are highly dependent on geologic time period and spatial location. While

the focus of the present work is in the central Andes, the methodology may be easily altered to apply to other regions in the world. The estimation of uplift rates world-wide is in itself an important undertaking. High uplift rates are indicative of slope failure and seismic hazards that often result in landslides, which can be highly destructive to human and ecological life (Kirby et al., 2008). In this manuscript, we propose a simplified methodology for observing the relationship between precipitation and orogenic evolution that relies on a Bayesian hierarchical modeling framework coupled with a general application of SPEL under steady-state assumptions. The main objective is to test the link between climate and landscape evolution by first developing a characteristic spatial scale that captures the interplay of these two effects and then using data at this scale to estimate uplift rates. We compare the estimated uplift rates to previously-measured values from the literature along with placing our results in the context of regional geomorphologic behavior. The utility of this method is its simplicity as well as its ability to recover key physical parameters of the system.

1.2 Research Goals and Objectives

The overarching goal of this thesis is to investigate the role regional climate plays on landscape evolution in orographic regions. The region we choose to focus on is the central Andes which is believed to have a strong relationship between climate and orogeny. To meet the ends of the research goal, the objective is to explain basin hypsometry by demonstrating the effects of distinct precipitation regimes on basin scale geomorphology. We propose to do this by constructing a physically-based Bayesian hierarchical model that will estimate uplift rates at a natural, sub-basin spatial scale. To prepare for proper model specification, a thorough geomorphologic analysis of the central Andes study region is conducted that includes an investigation of landscape self-organization and hypsometric analysis. Additionally, we investigate the spatial

and temporal organization of precipitation in the region to better understand climate dynamics. Initial analyses lead to three main hypotheses:

1. Similarities in spatial distributions of Strahler order 1 outlets and precipitation features by elevation are a first-order constraint on orographic evolution in the region.

2. Elevation classes determined by how landscapes self-organize provide a natural scale for assessing the relationship between climate and mountain building.

3. A Bayesian hierarchical modeling approach to physical systems can be appropriated to test the first two hypotheses.

The motivation behind employing a Bayesian hierarchical model is to estimate uplift rates from the physical SPEL model under steady-state assumptions. These uplift rates provide a means of comparing geomorphologic behavior between and within basins. The primary contribution of the research summarized in this thesis is the development of a simple physical-statistical model based on SPEL that provides reasonable estimates of regional uplift.

1.3 Thesis Outline

The presentation of the thesis is organized as follows. Chapter 2 describes the data obtained and utilized, gives a general description of the chosen study area, and presents the scaling scheme introduced for analysis. In this chapter we also conduct some preliminary data analysis using standard geomorphology methods. Chapter 3, presents initial findings that are promising indicators that precipitation and orogeny are influencing one another within the central Andes study area. Chapter 4 gives a thorough overview of the physical-statistical model developed to explore the proposed relationship. Results from the physical-statistical model, along with a discussion

that places the results in context with the prior analyses conducted in Chapters 2 and 3 and previously measured uplift rates in the Andes, are provided in Chapter 5. Concluding remarks are given in Chapter 6.

2

Methodology and Preliminary Data Analysis

A primary goal of the present research is to observe interactions between climate and landscape evolution in the central Andes at the water basin scale. For this work, we acquire data from a vast number of sources, including digital elevation maps (DEMs) for delineating watersheds and remote sensing data to analyze and characterize the climatology of precipitation in the region. The interdisciplinary nature of this project requires borrowing data analysis tools and methodologies from a number of fields in order to identify watersheds in the proposed study area, develop a *natural* scale to investigate geomorphological processes, classify basins based on well-established heuristics in geomorphology, and develop a physically-based statistical model to test hypotheses about landscape behavior. The purpose of this chapter is to provide an in depth discussion of the methods appropriated for carrying out these tasks. We begin with a discussion of delineating watersheds in the central Andes region from a high-resolution DEM. Next, we explain a scaling scheme we develop based on how elevations are distributed within the basins. Then, a thorough overview of hypsometry, a long-established practice of classifying morphologic stage of geologic development, is given as well as an application of this method to the watersheds

delineated in the study area. The satellite and rain gauge data used to provide an indication of regional climatic processes is described in the following section, along with how a correction for satellite-estimated mean annual precipitation (MAP) is calculated. Finally, as a large component of this work is testing hypotheses about landscape evolution with a physically-based Bayesian hierarchical model, the final section of this chapter is devoted to discussing the underlying physical model – the stream power erosion law (SPEL).

2.1 Identification of watersheds in the central Andes

In this section, we give an overview of the data and techniques used to identify watersheds in the central Andes study region that falls within 5-20S and 65-80W.

2.1.1 DEM data acquisition and pre-processing

In order to delineate basins in the central Andes study region, DEMs with 3-arc-second (~90m resolution) were acquired from U. S. Geological Survey (USGS) HydroSHEDS. The DEM grids were downloaded for the rectangular area 5-20S and 65-80W. Before delineating streams and basins, the DEM required processing using ArcGIS software. The steps for processing the DEM are as follows. First, the raw DEM grid cells are merged into one mosaic. The downloaded DEMs are unprojected, so a projection must be defined for the data. We choose the Lambert Conformal Conic Projection which is well-suited for large extents. Sinks, anomalous pits in the raw DEM data, are filled.

2.1.2 Stream and basin delineation

Streams and basins are delineated for the entire DEM extent using a common procedure in ArcGIS. This procedure consists of calculating flow direction and accumulation using the standard ArcGIS tools. To identify steams and basins, these tools

rely on calculating slope angles and directions for each cell in the DEM and then determining flow paths based on maximum change in elevation between proximate cells. We identify stream order using the Strahler ordering method (Strahler, 1957). Under this classification scheme, headwater streams are order 1. Two order 1 streams combine to make an order 2 stream. Two order two streams combine to make an order 3 stream and so on. The meeting of two streams of different orders results in a stream with the same ordering as the highest order stream (i.e. an order 2 and an order 3 combine to make an order 3 stream). To delineate basins, outlets are identified for every stream in the study area by snapping point features to the end of each stream. An area threshold minimum of $10km^2$ is used to delineate the smallest basins of Strahler order 1. This course resolution for delineating streams limits the headwater streams identified to mostly active streams. The threshold also keeps consistency with the length scale of the precipitation data used as a climate proxy. To ensure consistency with higher order streams, we compare the streams delineated here to the dataset of world streams provided by the USGS and find agreement in the locations of streams identified. Basins are classified by the Strahler method as well.

We divide our original study area into three distinct regions representing northern, central, and southern portions marked by 5-10S, 10-15S, and 15-20S, respectively. Within these regions, we focus on two order 6 watershed in the north, one order 7 and an order 5 watershed in the center, and two order 7 watersheds in the south (Figure 2.1). The two basins identified in the northern region are the Marañón-2 and Huallaga-1. The Ucayali, the largest of the river basins, is the order 7 basin and Madre de Dios, the smallest, is the order 5 watershed located in the central region. The Beni-2 and Salar de Uyuni river basins are located in the southern region. For each area, all smaller order watersheds were delineated as well.

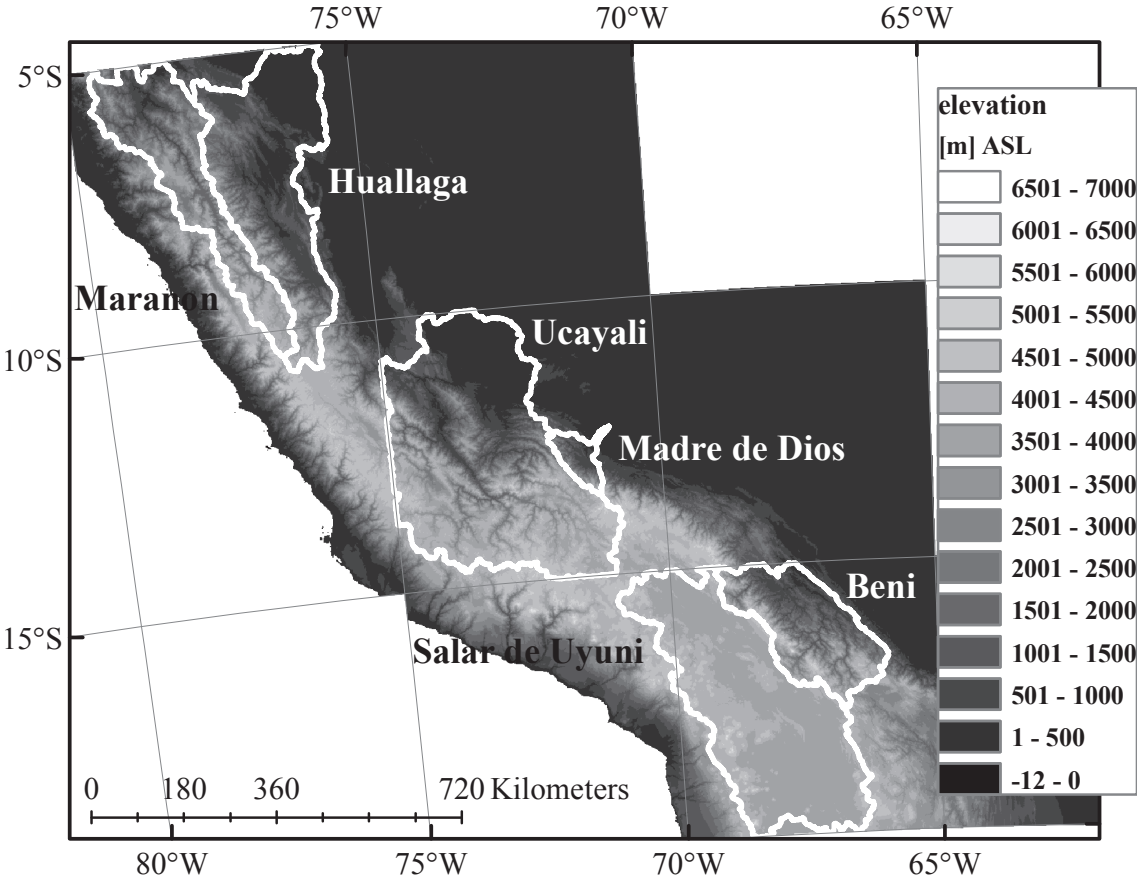

FIGURE 2.1 The central Andes study region considered for analysis. The Huallaga and Marañón make up the watersheds of the northern region (approximately between 5S and 10S), The Ucayali and Madre de Dios are located in the central region (between 10S and 15S), and the Salar de Uyuni and Beni basins fall within the southern region (between 15S and 20S).

2.2 Elevation Class Development

To examine local geomorphology within each basin, we develop a characteristic spatial scale which we refer to as an elevation class. We propose that the elevation class will give an indication of how the landscape is self-organized and provide a natural scale to observe the interactions of climate and tectonics within each basin. These elevation classes are based on topographic self-organization within a given watershed. To determine the range of the elevation classes for each of the six basins displayed

in Figure 2.1, we first create histograms of the outlet elevations for the different Strahler orders. These are all binned by 10m intervals. The elevation classes are determined by observing peaks in the distributions (Figure 2.2). We hypothesize that these peaks mark the separation of distinct elevation regimes with different geomorphological behaviors. The specific intervals for the elevation class divisions determined for all six watersheds are given in Table 2.1.

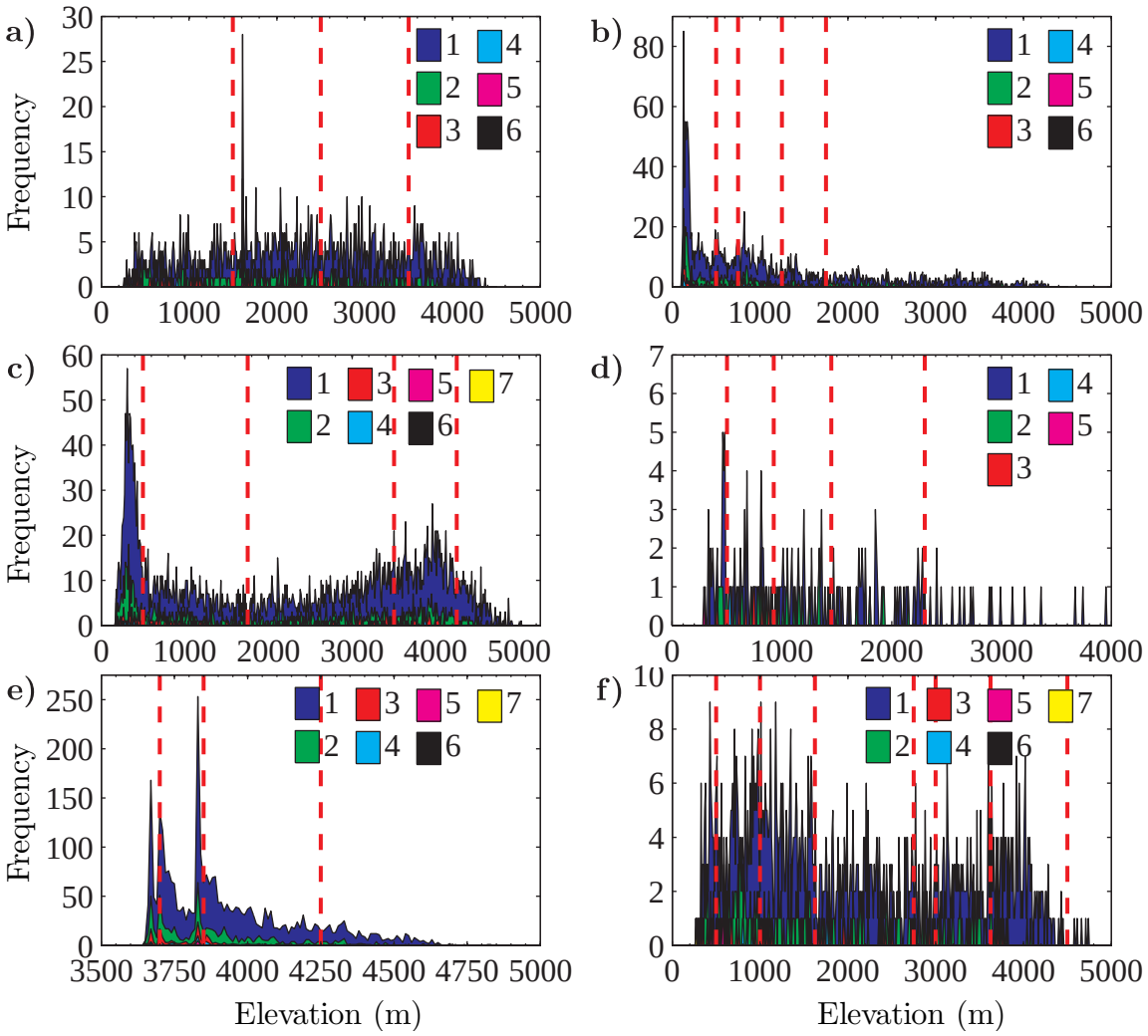

FIGURE 2.2 Histograms of outlet elevation by Strahler stream order for the six watersheds in the central Andes with bins every 10m. The dashed red vertical lines mark the divisions of the elevation classes. The divisions were chosen by identifying distinct peaks in the elevation distributions. a) Marañón. b) Huallaga. c) Ucayali. d) Madre de Dios. e) Salar de Uyuni. f) Beni.

Table 2.1 The elevation class divisions of the central Andes watersheds.

Elev. Class	**Marañón**	**Huallaga**	**Ucayali**	**Madre de Dios**	**Salar de Uyuni**	**Beni**
1	<1500m	<500m	<500m	<500m	<3700m	<500m
2	$1500-2500$m	$500-750$m	$500-1750$m	$500-925$m	$3700-3850$m	$500-1000$m
3	$2500-3500$m	$750-1250$m	$1750-3500$m	$925-1450$m	$3850-4000$m	$1000-1625$m
4	>3500m	$1250-1750$m	$3500-4250$m	$1450-2300$m	>4000m	$1625-2750$m
5	–	>1750m	>4250m	>2300m	–	$2750-3000$m
6	–	–	–	–	–	$3000-3625$m
7	–	–	–	–	–	$3625-4500$m
8	–	–	–	–	–	>4500m

2.3 Hypsometric Analysis

Hypsometry is a valuable tool for characterizing and understanding the evolution of landscapes. Here a complete review of the techniques common to the practice as well as the interpretations of hypsometric analysis are discussed. The fundamental graph is known as a hypsometric curve and is useful in determining the dominant morphologic process at hand – whether erosion or uplift is governing landscape evolution. The area under this curve is known as the hypsometric integral and gives a quantification of the morphologic age of the landscape. After a discussion of these techniques, we demonstrate an application of the tools with the basins identified in the central Andes region.

2.3.1 Overview of technique and interpretation

The hypsometric curve is a long established practice in geomorphology that demonstrates how elevations are distributed within a hydrologic unit. It provides insight into the geomorphologic processes that are dominant within a region (Strahler, 1952). With the advent and DEMs and geographic information systems to process them, hypsometry has become readily accessible practice. Hypsometric curves are simple graphs where elevation is plotted against cumulative area. Thus, at any point along the hypsometric curve, one envisions an elevation contour and the entire area that lies above that contour. These curves are typically interpreted by regions of curvature denoted by inflection points. Strahler (1952) discusses the significance of inflection points along hypsometric curves, which mark the elevation at which the rate of decreasing mass changes. The interpretation is relatively straightforward. Instances where the hypsometric curves are concave reflect the percent elevation and area of a given basin that are dominated by fluvial erosion processes. In contrast, the areas and elevations where the curves are convex demonstrate regions where tectonic uplift

is the prominent process (Montgomery et al., 2001).

An important quantity in hypsometry is the hypsometric integral, which is defined as the area underneath the hypsometric curve. A simple approximation of the hypsometric integral (HI) is given by $HI = (H_{mean} - H_{min})/(H_{max} - H_{min})$, where H denotes basin elevation (Brocklehurst and Whipple, 2004; Cohen et al., 2008; Pérez-Peña et al., 2009). Strahler (1952) notes the importance of the hypsometric integral in determining the morphologic stage. Integrals that fall between 40-60% are described as existing in a stage of equilibrium. These are mature watersheds that are in steady-state with regards to erosional process due to fluvial systems and tectonic resistance. A monandock phase is a conspicuous, unsteady phase that exhibits abnormally low hypsometric integrals ($< 35\%$). Finally, the author claims the younger, also inequilibrium, stage transitions at hypsometric integrals of 60% to the mature, equilibrium stage. These classifications of morphologic ages, however, have come into question in recent years. Willgoose and Hancock (1998) show that the morphologic stages described by Strahler (1952) based on hypsometric integral values are less a measure of maturation and more an indication of differing catchment topology and geometry. Though this discrepancy in interpretation exists, the main point here is that both sets of authors agree that differences in qualitative behavior exist and are determined by the quantitative values of the hypsometric integrals. Groupings based on both the hypsometric integral and curves will be used as a preliminary means to qualify differences in geomorphologic behavior in the central Andes watersheds.

2.3.2 Application to basins in central Andes

We construct hypsometric curves for the six basins within our study region using elevation and area data derived from the processed DEMs. The hypsometric curves are displayed in Figure 2.3. It is evident that each basin has a distinct curvature and there are no shared regional similarities. Although this result differs from the

findings of Montgomery et al. (2001) who showed regional similarities in hypsometry within areas located in the northern, central, and southern Andes, this disagreement is expected. The areas of study considered in the present manuscript differ considerably from that used by Montgomery et al. (2001) in both size and scale. In the aforementioned work, the authors conduct a hypsometric analysis of parallel slices over the Andes. These slices are both larger in size and different in organization as compared to the basins we consider. As a result, we do not find regional agreement in the shapes of hypsometric curves. This is consistent with the work of Willgoose and Hancock (1998), who demonstrate that the same landform and different scales will yield different hypsometric curves. These authors also note that basin shape has an impact on the resulting hypsometry.

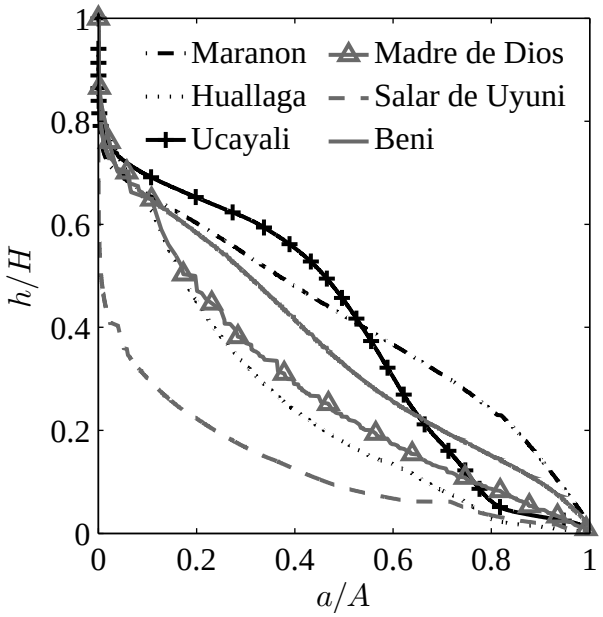

FIGURE 2.3 Hypsometric curves for the six watersheds in central Andes study area.

By evaluating the inflection points and curvature of the hypsometric curves, we may determine the dominant geomorphologic processes controlling the basins. We see that a large portion of the Huallaga, Madre de Dios, and Salar de Uyuni basins are undergoing fluvial erosion. The Ucayali basin is largely under the influence of

tectonic uplift. The Marañón and Beni basins both appear to fall somewhere within a balance of fluvial erosion and tectonic uplift, given the flatter nature of their hypsometric curves.

We also compute the hypsometric integrals for the six basins using the simplified method described previously. The results are listed in Table 2.2. Besides the Madre de Dios, all of the basins have integrals that fall between 40-60%, which Strahler (1952) would describe as within an equilibrium stage, while Willgoose and Hancock (1998) would claim that the basins are under the influence of geomorphologically similar processes. Again, our main interest is that these basins are exhibiting similar behavior. Recall, that another distinction existed for basins with hypsometric integrals of 60%. Strahler (1952) described these watersheds as transitioning from younger, inequilibrium stages of development to more mature stages. Conversely, if we were to consult Willgoose and Hancock (1998) a basin with such an integral would represent one that is undergoing a qualitatively different process than the basins with integrals that fall between 40-60%. We see that two basins within the study areas fall under the category of hypsometric integrals of 60%, the Marañón and Beni, while three basins, Huallaga, Ucayali, and Salar de Uyuni have integrals near 50%. The Madre de Dios basin has a high hypsometric integral of 75% and would be considered in a young, inequilibrium stage by Strahler (1952). To summarize what we have observed, basins that were found to have similar hypsometric curves, and thus undergoing similar geomorphologic processes, also have similar hypsometric integral values, except for the Ucayali and Madre de Dios basins. However, the fact that the Madre de Dios basin may be under an inequilibrium stage of development may limit the applicability of the steady-state assumption we make when estimating uplift rates.

Table 2.2 Hypsometric integrals for central Andes watersheds approximated using simplified method.

Basin	HI (%)
Marañón	59.93
Huallaga	50.91
Ucayali	50.88
Madre de Dios	75.51
Salar de Uyuni	48.54
Beni	59.71

2.3.3 Elevation classes and hypsometric curvature

To evaluate how landscape self-organization relates to hypsometry, we plotted the hypsometric curves once more, but with the elevation classes determined from the previous section marked for each basin. Figure 2.4 shows the location of the elevation classes, determined from the histograms of outlet elevations for each watershed (see Figure 2.2). Since the elevation classes were determined by how elevation is organized within each basin, we see in Figure 2.4 how this characteristic spatial scale relates to hypsometry. For each watershed, the elevation classes mark regions of distinct curvature along the hypsometric curves, exhibiting either a convex or concave nature. Thus, the elevation classes appear to distinguish regions undergoing distinct geomorphological processes as well.

2.4 Remote Sensing Data for Precipitation Analysis

Precipitation data used in this study comes from the Tropical Rain Measuring Mission (TRMM) satellite between 1998 and 2011. We use both TRMM precipitation features (PFs) (provided by the University of Utah) and the TRMM 3B42 version 7 combined instrument product. Here, we give an overview of these products, including sources of error and limitations.

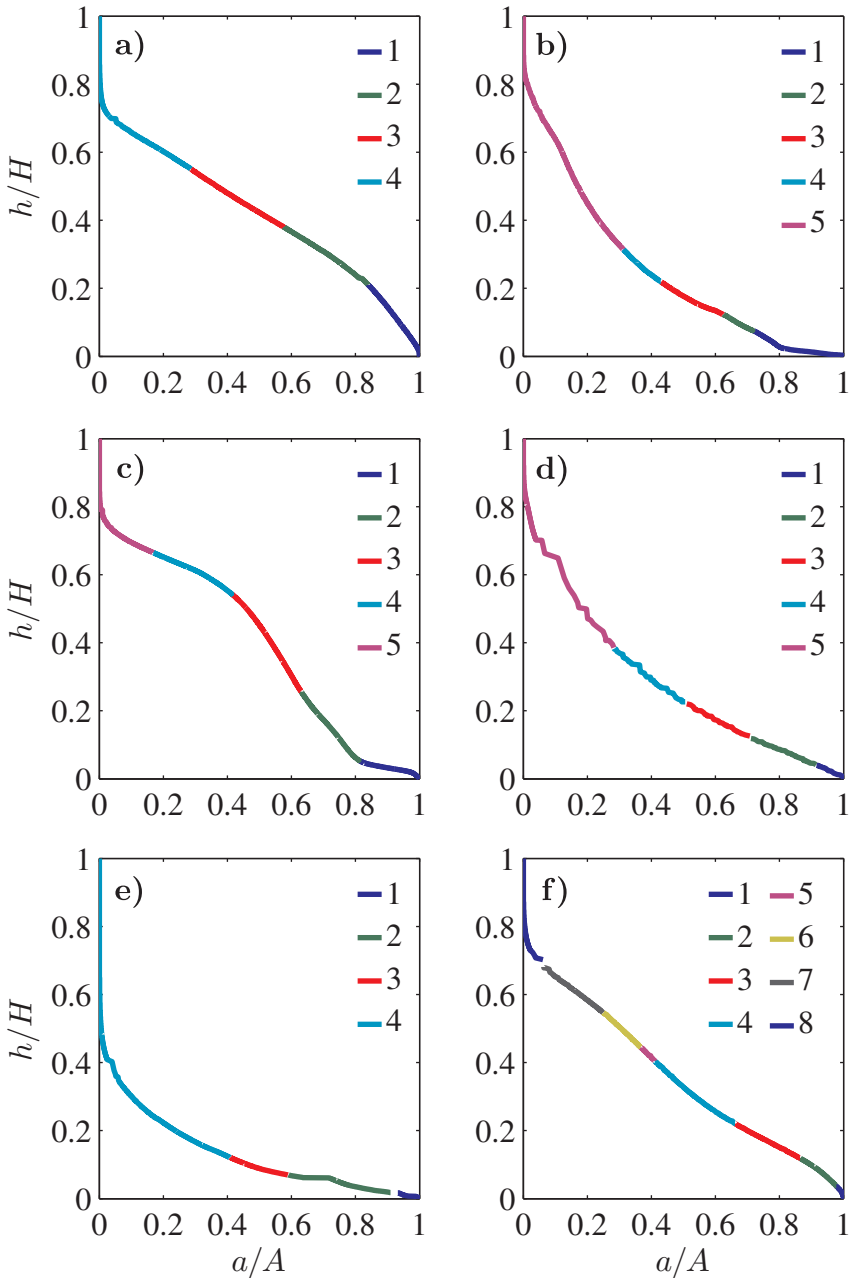

FIGURE 2.4 Hypsometric curves marked by elevation class for the six watersheds in the central Andes study region. a) Marañón. b) Huallaga. c) Ucayali. d) Madre de Dios. e) Salar de Uyuni. f) Beni.

2.4.1 TRMM PFs

TRMM PFs are a product derived from the TRMM microwave imager (TMI) and precipitation radar (PR) sensor data and are available at 75 km^2 resolution. The algorithm used to identify precipitation features was first adapted by Nesbitt et al. (2000). The idea is to use the TRMM PR 2A25 near-surface reflectivity and the TMI polarization corrected temperature in order to classify PF size and intensity. TRMM PF data is useful for identifying the location, frequency, and intensity of individual storms. One limitation of this product is its coarse spatial resolution. Additionally, the product reports volumetric rain rates which give a sense of the intensity of rainfall, but cannot be used to determine specific amounts of total rainfall for a given storm event. However, TRMM PFs have the specific advantage of distinguishing precipitation over complex terrain, where individual products like TRMM 2A25 tend to underestimate its occurrence in mountainous regions. Thus, using a product that better resolves storm events in the central Andes will be critical in order to evaluate spatial and temporal patterns of precipitation in the region. For this study, we obtain a 14-year climatology of TRMM PFs and use the centroids to determine the location of specific storm events over the central Andes study area.

2.4.2 TRMM 3B42 version 7

The TRMM 3B42 v.7 product is a gridded product that provides calibrated 3-hourly rain rates based on orbit data from the visible infrared scanner (VIRS) and TMI and merged infrared precipitation data from multiple satellite instruments including the Special Sensor Microwave Imager (SSM/I), the Advanced Microwave Scanning Radiometer-Earth Observing System (AMSR-E), and the Advanced Microwave Sounding Unit-B (AMSU-B). The level 3 product is available at a 0.25 by 0.25 degree resolution. The TRMM 3B42 product allows for direct calculation of regional precipitation accumulations. A limitation of this product, however, is its tendency

to underestimate precipitation over complex terrain and, specifically, its inability to capture peaks in precipitation over the Andes (Bookhagen and Strecker, 2008; Barros, 2013). This product is used to compute conservative estimates of mean annual precipitation (MAP) for the central Andes study region. These estimates will be an underestimation of the true MAP in the region, thus we use rain gauge data from the Kospiñata network in Peru, located within the Madre de Dios basin, to determine a correction.

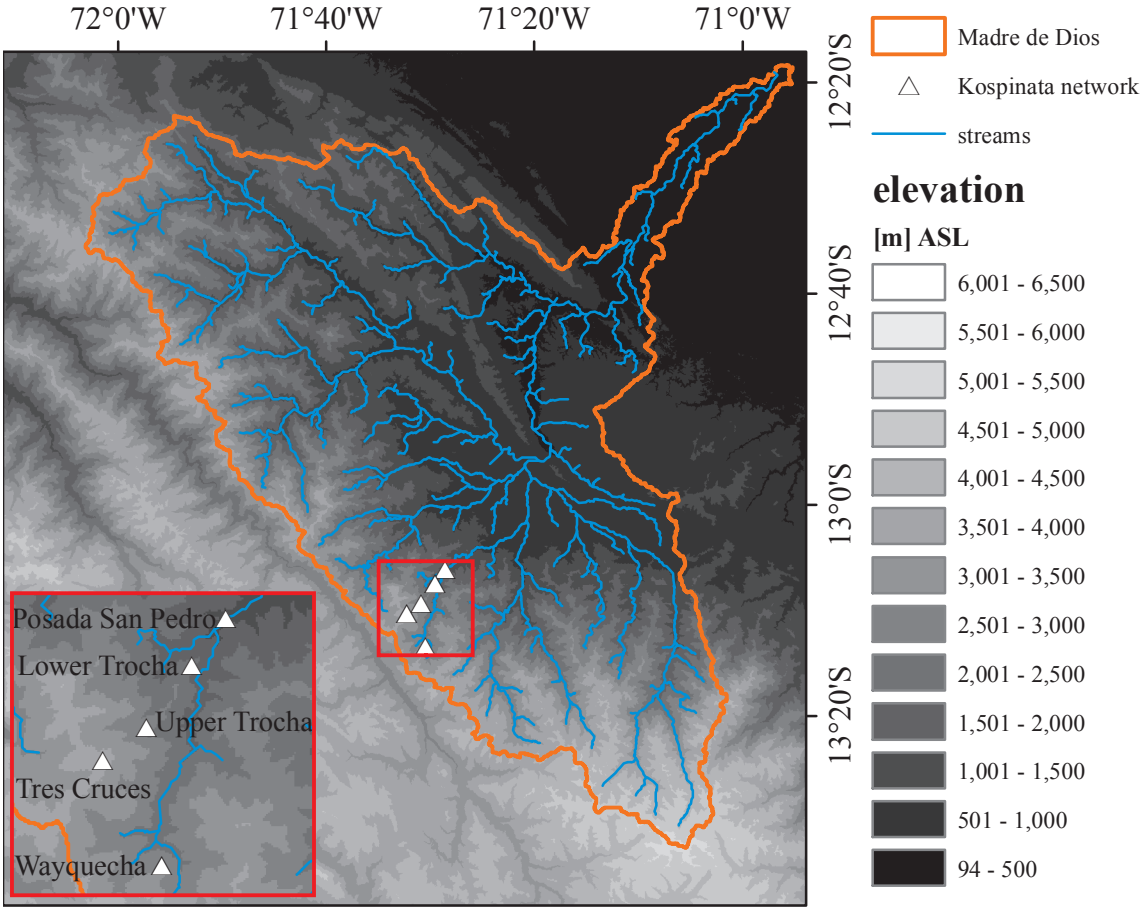

FIGURE 2.5 Rain gauges of the Kospiñata network located in the Madre de Dios river basin. These gauges are located in the higher range of elevations of this watershed.

2.4.3 Orographic adjustment for TRMM 3B42 v. 7

The underestimation of the TRMM 3B42 3-hourly precipitation rain rates has been well-documented (Bookhagen and Strecker, 2008; Barros, 2013). For this reason, we calculate an orographic adjustment for the TRMM mean annual precipitation (MAP) data via ordinary least squares (OLS) regression with the Kospiñata rain gauge network in Peru. The Kospiñata network lies in the Madre de Dios basin (Figure 2.5). While the specific measurements of MAP at given elevations by the rain gauges will not be exact for the other basins, using this data as a supplement provides an upper bounds to the uncertainty we have in each basin's regional climate. Thus, using both MAP estimates from the TRMM 3B42 product and the correction using the rain gauge data gives a quantification of the range of uncertainty we have for climate in terms or precipitation. Since we computed MAP with the TRMM data for specific elevation classes, the regression is conducted between the TRMM MAP for a given elevation class and the rain gauge MAP located at an elevation within the elevation class. If more than one rain gauge is located within the range of a single elevation class, we average the MAP values. Figure 2.6 shows the results of the OLS regression and the resulting equation which is used to calculate the orographic adjustment. We are unable to determine an orographic adjustment for the Salar de Uyuni basin, because only one rain gauge from the Kospiñata network falls within the elevation range of this basin. Additionally, since the Andean Plateau is known for its arid climate, adjusting the MAP for the Salar de Uyuni based on rain gauge data collected from the Eastern Cordillera would not be meaningful. The rain gauge data applicable to the Huallaga basin is also limited, only two points, and so we do not have great confidence that the adjusted value reflects actual MAP in the region. However, we do believe that the corrected value will give a better range that captures regional climate than the TRMM 3B42 product alone.

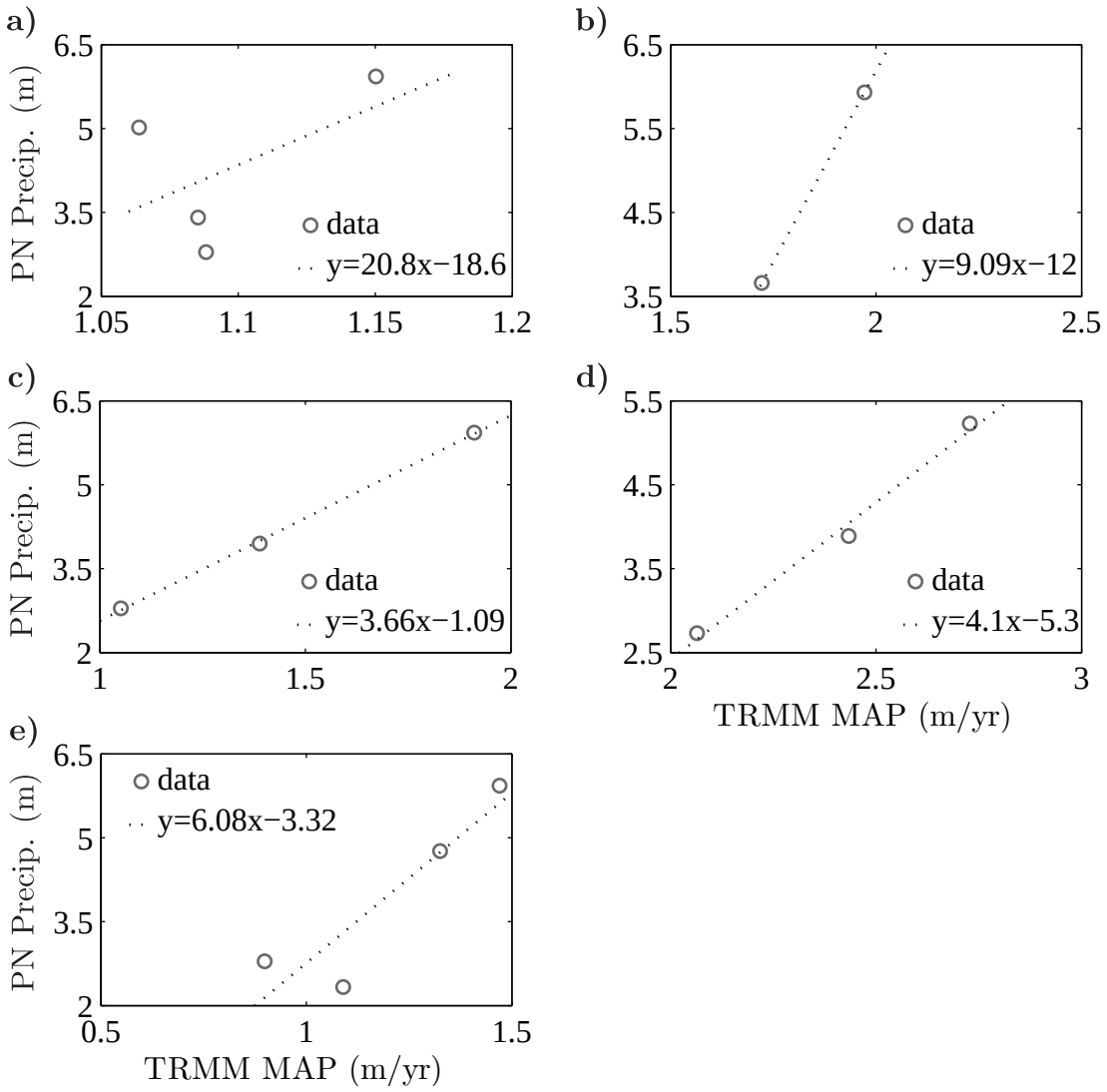

FIGURE 2.6 The TRMM 3B42 product severely underestimates precipitation in orographic regions. Using data from the Kospiñata rain gauge network in Peru, located in the Madre de Dios basin, we calculate an adjustment for the TRMM MAP calculated previously using the linear fit. a) Marañón. b) Huallaga. c) Ucayali. d) Madre de Dios. e) Beni.

2.5 Steady-state Stream Power Erosion Law (SPEL)

A basic physical model used to describe erosional processes in orographic regions is the stream power erosion law (SPEL). SPEL is an empirical power law that describes erosion in terms of change in relief along a stream channel and channel discharge,

i.e.,

$$E = K \left(\frac{dz}{dx} \right)^n Q(x)^m \ , \tag{2.1}$$

where E is the erosion rate, dz/dx is the channel slope, K is the erosion coefficient, Q is the discharge, and m and n are empirically-derived exponents that correspond to regional differences in erosion and climate processes. The valid range for m and n values are generally positive and their ratio is typically taken to be near 0.5 (Gasparini et al., 2007). Under steady-state assumptions, erosion is said to balance uplift (i.e. $E = U$), and the form of the power law becomes

$$\frac{dz}{dx} = \left(\frac{U}{K} \right)^{1/n} Q(x)^{-m/n} \ , \tag{2.2}$$

where U is the (constant) uplift rate. The appropriation of a constant uplift term rests on the consideration of regions that are small with respect to geologic time scales (Moglen and Bras, 1995). The steady-state assumption that erosion is everywhere balanced by uplift is typically widely applicable. It is commonly assumed that landforms are statistically invariant over long geologic time periods (Whipple, 2004).

2.5.1 Main assumptions of steady-state SPEL

The claim that erosion is equal to uplift in the formulation of steady-state SPEL is based on long-term orogen behavior over geologic timescales. This requires that local erosion must be balanced by the rock uplift rate in all areas of a region of study (Whipple and Tucker, 1999). SPEL in its most basic form is applicable at the orogen scale (Whipple and Meade, 2004). However, in its steady-state application Whipple and Meade (2004) postulate that within this regime three main assumptions are required: 1) channel profiles in equilibrium follow the power law relationship similar to

$$\frac{dz}{dx} = kA^{-\theta} \ , \tag{2.3}$$

where dz/dx is the channel slope, k a constant of proportionality, A the drainage area, and θ the concavity index; 2) k has a power law relationship with rock uplift and erosional efficiency; and 3) rock uplift and erosional efficiency have no impact on the concavity index, θ. Often, under steady-state assumptions this concavity index is given by the ratio of the dimensionless exponents m and n: $\theta = m/n$, and this may be used to determine inputs for these parameters (Finlayson and Montgomery, 2003). However, if a strong orographic precipitation effect is present, this relationship no longer holds, and m and n cannot be readily determined (Roe et al., 2002).

2.5.2 Incorporation of climate effects

Often the discharge term is simplified by considering it to be proportional to upstream drainage area through some constant of proportionality (e.g., Stock and Montgomery, 1999; Whipple and Tucker, 1999; Sklar and Dietrick, 1998); however this immediately precludes the possibility of considering the effects of climate on stream channel evolution (Wu et al., 2006; Roe et al., 2003, 2002). In order to account for variable erosional processes due to differences in precipitation patterns, a number of authors have accounted for climate by altering the discharge term in SPEL. Roe et al. (2003) approximate discharge along a stream channel with spatially uniform precipitation up to some given location along the stream channel where they introduced a precipitation anomaly. They find the impact on change in channel relief is highly dependent on where the precipitation anomaly occurs. When the anomaly is near the channel head, cumulative discharge increases and change in relief is much higher than when the anomaly occurs near the end of the channel. Roe et al. (2002) incorporate an orographic precipitation feedback into the discharge term and show that this feedback produces a first-order effect on the outcome of stream channel concavity. Wu et al. (2006) adapts the geomorphoclimatic instantaneous unit hydrograph, first developed by Rodríguez-Iturbe et al. (1982) to test the sensitivity of SPEL to various precipita-

tion parameters including frequency, intensity and duration. The authors find that the resulting channel profile is most sensitive to precipitation intensity. These studies demonstrate that simply considering the effects of precipitation have huge outcomes on stream channel evolution when using SPEL as the base model to explain erosional processes. Thus, for the present exploration of climate-tectonic interactions in the central Andes we will incorporate the effects of precipitation through the discharge term.

3

Evidence of Orographic Enhancement of Precipitation

A key component of the research conducted in this manuscript is the incorporation of climate effects in the form of precipitation into a physical model as a control on erosional processes. As justification for this major consideration, we dedicate this chapter to an investigation of an enhanced orographic precipitation effect in the central Andes study region. The goal is to demonstrate the strong ties that persist between spatial and temporal precipitation patterns and landscape organization at the basin and sub-basin scale. We begin with a discussion of how the spatial and temporal occurrence of precipitation is controlled by the mountain landscape of the Andes. We then present an interesting qualitative similarity in how precipitation and first order outlets are distributed by elevation and conduct a preliminary analysis on its significance that will later be considered in the physical-statistical model.

3.1 Spatial and temporal patterns of precipitation

The spatial occurrence of precipitation in Central Andes is arranged in a fairly regular manner. Using TRMM PF data, Giovannettone and Barros (2009) found that during the early evening, storm events are generally concentrated along the ridges of the Andes, while during the early morning they are clustered along valleys and slopes. We use a 14-year climatology of TRMM PF data and find this same diurnal pattern at the smaller, basin scale within the study area (Figure 3.1c). We also note higher frequency in precipitation during the afternoon and evening relative to during the early morning. These descriptions of precipitation behavior are summarized in Figure 3.1, which shows the centroids of the PFs during the early morning and evening that occur over the Marañón and Huallaga basins. During the early morning, 1am-7am, precipitation events occur primarily in the valleys. In the afternoon and early evening, 1pm-7pm, they are concentrated along the ridges. Additionally, there is a higher amount of PF occurrences in Figure 3.1b relative to Figure 3.1a, indicating a larger number of storms during the afternoon/evening.

Another key finding of the analysis of the temporal distribution of precipitation is a cyclical behavior in the movement of precipitation from lower elevations during the morning to higher elevations during the evening. Figure 3.2 shows this diurnal behavior during both wet and dry months for the Marañón basin. During the morning hours, precipitation events occur mostly at low elevations. Throughout the day, they migrate from low elevations to high elevations. In the evening, these events occur primarily at high elevations. At night, there is a movement of precipitation events towards lower elevations. This particular diurnal pattern exists in all six basins and, again, is in agreement with the findings of Giovannettone and Barros (2009), who found this same pattern at the larger, mountain range scale. The evidence here provides support that orography is heavily influencing and modifying the spatial and

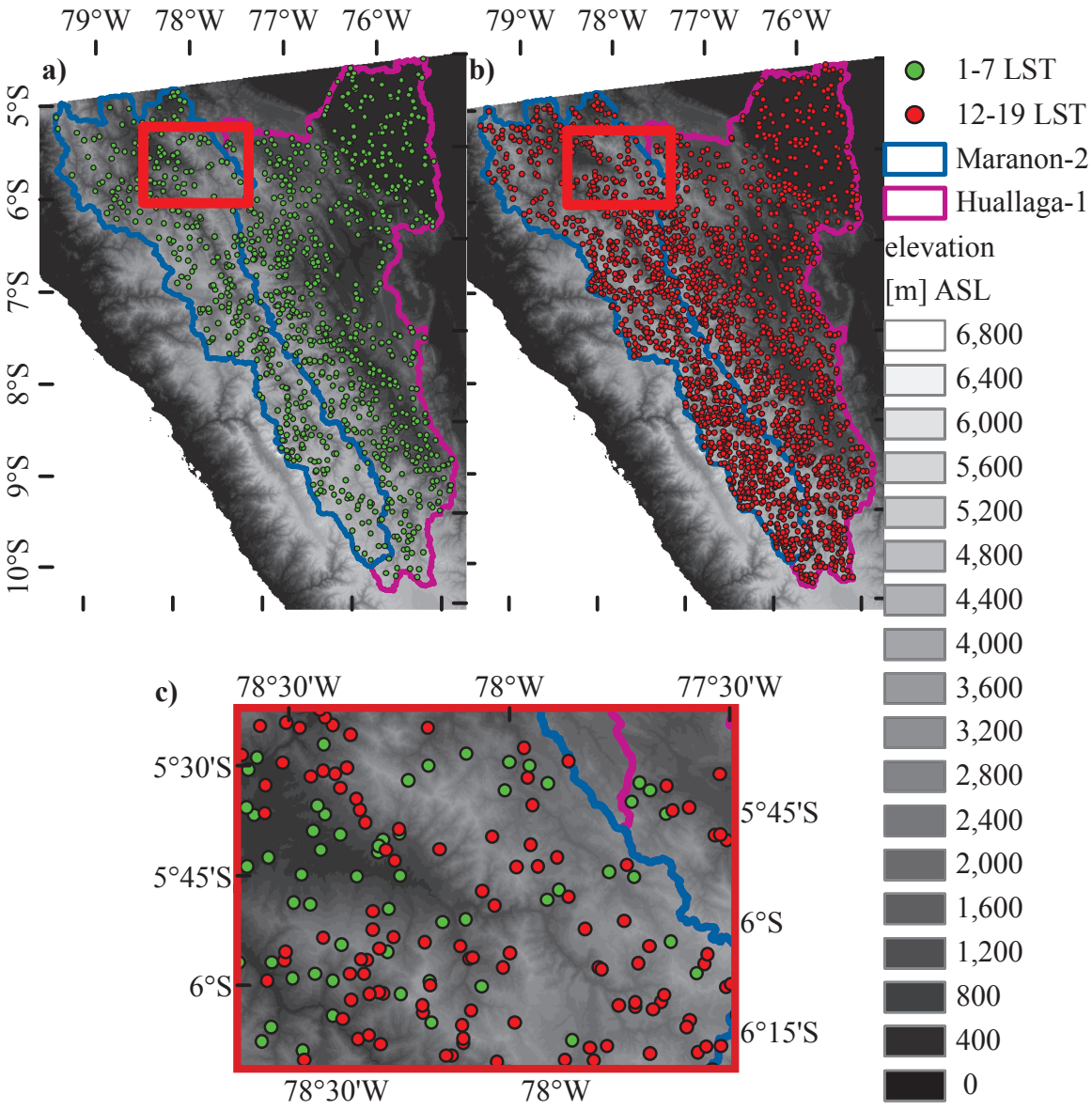

FIGURE 3.1 a) TRMM precipipation features that occurred between 1am and 7am between during the 14-year climatology. b) TRMM precipitation features that occurred between 12pm and 7pm during the 14-year climatology. c) Zoomed-in view to demonstrate the how precipitation is spatially organized at different periods of the day. Notice that during the night, most precipitation features are located on the ridge tops, while during the day they primarily occur in along the slopes and valleys.

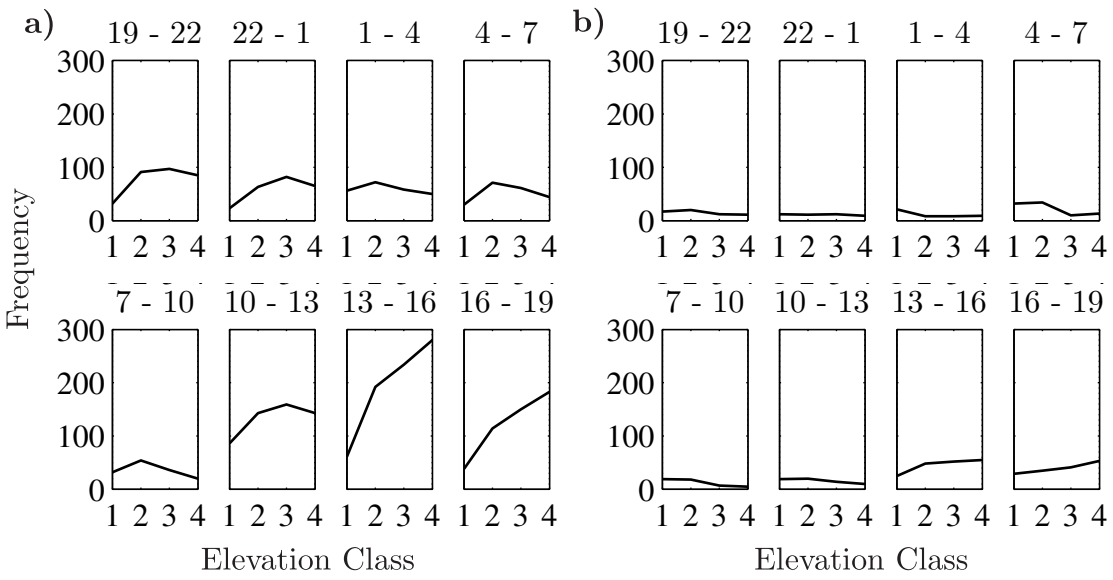

FIGURE 3.2 a) March 1998-2011. b) August 1998-2011. Diurnal organization of precipitation in the Marañón basin using TRMM PF data for March and August 1998-2011. While there is an increase in precipitation during the wet season (March) relative to the dry season (August), the cycle of peak occurrences remains similar year-round. During the transition from night to day (top rows) peak precipitation occurs primarily in the lower elevation classes, while during the transition from day to night (bottom rows) it moves to the higher elevations.

temporal organization of precipitation in the central Andes.

3.2 Link between first order outlets and precipitation features

By observing the distribution of the TRMM PFs by the ground surface elevation over which they occur, a distinct relationship between atmospheric and geomorphologic processes becomes readily apparent. The histograms of first order outlet elevations (Figure 2.2) are remarkably similar to the histograms of the TRMM precipitation data, also binned by elevation (Figure 3.3). The spikes in frequency and overall shape of each distribution appear to be preserved in the histograms created with the PFs. The congruency of the peaks leads to a key finding here that the elevation classes devised earlier to describe landscape self-organization within the watersheds in the central Andes are also representative of distinct precipitation regimes. Thus, the hypsometric curves in Figure 2.4, not only denote classes of elevations, but also

those of precipitation. This embedded relationship of active fluvial erosion and precipitation/elevation regimes will be explored later through the parameterization of the physical-statistical model.

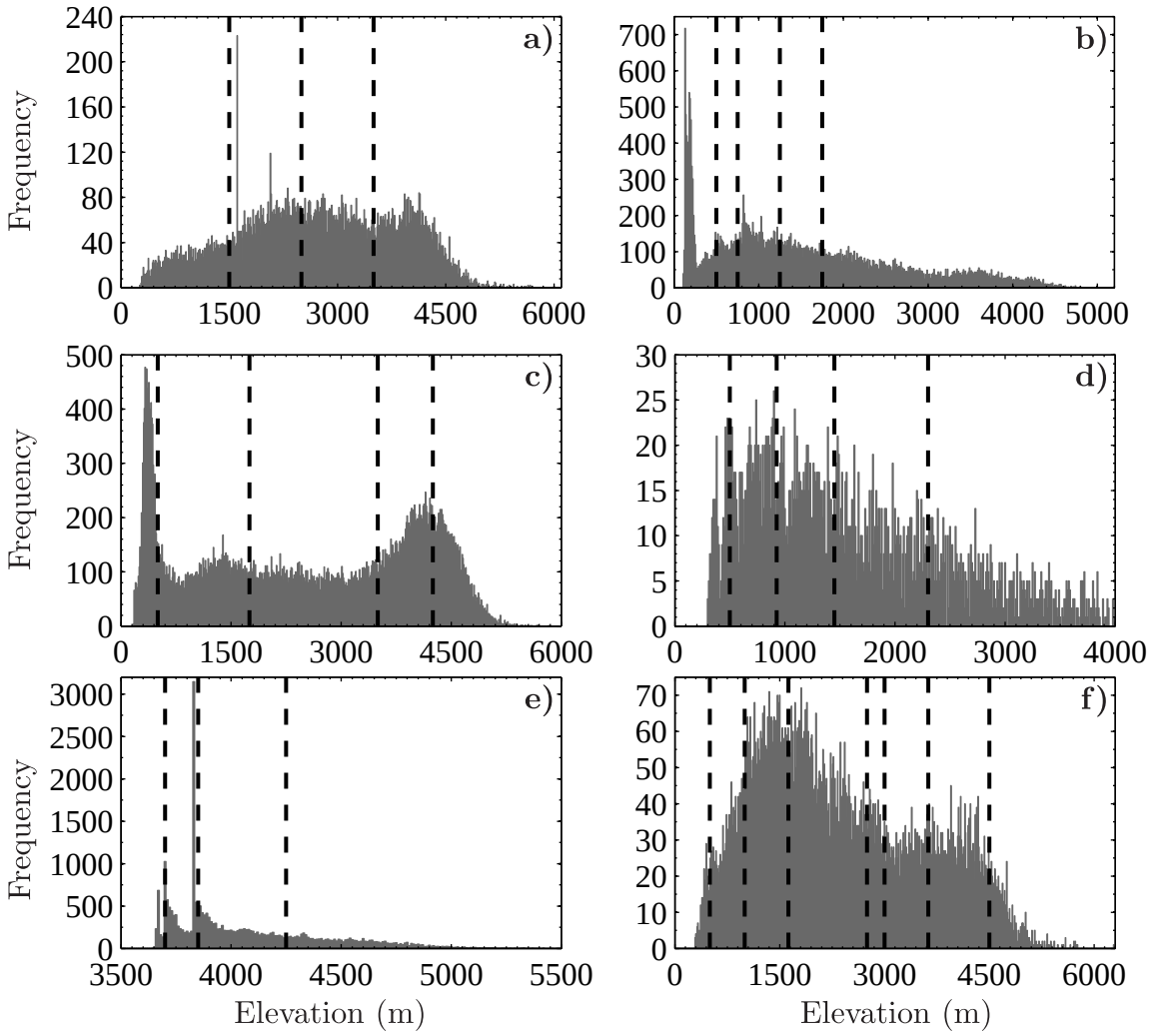

FIGURE 3.3 Histograms of TRMM PFs by elevation for the six watersheds in the central Andes with bins every 10m. The black vertical lines mark the divisions of the elevation classes. Note the similarities in the shapes of these histograms with those shown in Figure 2.2. The similarity between these two distributions indicates that the elevation class scale is adequate to capture the link between climate and tectonics. a) Marañón. b) Huallaga. c) Ucayali. d) Madre de Dios. e) Salar de Uyuni. f) Beni.

A first attempt to investigate the similarities between the distributions of first order outlets and precipitation events by elevation led to conducting cross-correlations

between the frequencies from the histograms of the first order outlets and precipitation events. We did this twice, once without normalizing and once with normalizing by the area to account for differences in the shapes of the watersheds. By normalizing by area, we are removing the contribution of the tectonic forcing, which influences basin structure, in the resulting similarities between first order outlets and precipitation. We refer to these different correlation coefficients as ρ^2_{op} and $\rho^2_{op,h}$, where the first refers to a correlation coefficient resulting from a cross-correlation between outlets and PFs and the second normalizes according to the basin structure. Table 3.1 displays the values of ρ^2_{op} and $\rho^2_{op,h}$ for each of the six watersheds. The results show relatively high correlation coefficients for all of the watersheds when not normalizing for shape. However, we see that normalizing for shape has a larger effect on the correlation coefficient for the Marañón, Ucayali, and Beni basins. This leads us to hypothesize that hypsometry, and thus tectonics, is playing a large role in the governing dynamics of these watersheds. We suspect that the other remaining watersheds, the Huallaga, Salar de Uyuni, and Madre de Dios have topographies that are predominantly controlled by climate-land dynamics.

Table 3.1 Cross-correlation coefficients.

Watershed	ρ^2_{op}	$\rho^2_{\mathrm{op,h}}$
Marañón	0.62	0.25
Huallaga	0.80	0.71
Ucayali	0.73	0.47
Madre de Dios	0.55	0.46
Salar de Uyuni	0.93	0.75
Beni	0.50	0.30

4

Development of Physical-Statistical Model

The final component required to test the previously determined hypotheses about landscape evolution in the central Andes is the development of a quantitative model that can capture climate and basin interactions at the elevation class scale developed in Chapter 2. We propose to do this by estimating the uplift rates in the steady-state stream power erosion law (SPEL), which may then be compared to previously measured values. Developing a model with a largely statistical component requires a note about notation. We express the probability of an event, a, as $P[a]$; the conditional probability of an event a dependent on the occurrence of another event b, as $P[a|b]$. And finally, the joint probability of two events a and b both occurring as $P[a, b]$. The goal of this chapter is to provide a brief explanation of how Bayesian hierarchical models can be employed for physically-based problems and a thorough demonstration of how this technique is applied to steady-state SPEL. In the accompanying appendices referenced in this chapter, we check the model diagnostics to ensure meaningful results are produced.

4.1 General framework: Bayesian hierarchical modeling for physically-based problems

The main goal in developing a physical-statistical model is to estimate uplift rates for the different elevation classes within each basin in the study area. This model is based on the idea of incorporating a physical process model within a Bayesian hierarchical framework. There is known utility in applying Bayesian methods to geoscience problems with the specific goal of estimating physically-relevant parameters (Allmaras et al., 2013; Calvetti and Somersalo, 2010; Berliner et al., 2008; Berliner, 2003; Berliner et al., 2000b; Campbell, 2004). This approach has been developed previously for a range of applications including predictions of tropical Pacific sea surface temperatures (Berliner et al., 2000b); modeling annual hurricane counts for the U.S. using the El Niño-Southern Oscillation and North Atlantic Oscillation as predictors (Elsner and Jagger, 2004); highly complex air-sea interactions using simulated data (Berliner et al., 2003); analytical diffusion models to predict relative abundances of bird species in the U.S. (Wikle, 2003); and evaluating the impacts of anthropogenic climate change forcings in the form of spatial CO_2 fingerprinting (Berliner et al., 2000a).

To construct a hierarchical model for physically-based problems, Bayes' theorem is employed to the joint probabilities of the variables and parameters in question. Suppose we have a physical process model M, data collected on this process D, some statistical error parameters Θ, and physical parameters η. Their joint probability will be given by

$$\begin{aligned} P[M, D, \Theta, \eta] &= P[D|M, \Theta, \eta] \times P[M, \Theta, \eta] \\ &= P[D|M, \Theta, \eta] \times P[M|\Theta, \eta] \times P[\Theta, \eta]. \end{aligned} \tag{4.1}$$

The factors on the right-hand side (RHS) the above equation are as follows: the first term is referred to as the data model, the second term is a prior physical process incor-

porating uncertainty, and the last term is a joint prior probability for the statistical and physical parameters. The data model term may be expressed as $P\left[D|M,\Theta\right]$, assuming that the data has no further dependence on physical parameters, a reasonable assumption (Berliner et al., 2008; Campbell, 2004). The prior process model is thought to have no dependence on the statistical parameters, as it is a representation of the purely physical model, and takes the form $P\left[M|\eta\right]$. In the prior parameter model, it is appropriate to assume that the physical and statistical parameters are *a priori* independent such that $P\left[\Theta,\eta\right] = P\left[\Theta\right] \times P\left[\eta\right]$ (Wikle, 2003). The joint probability of the variables and parameters from the physical model in question may now be expressed as

$$P[M, D, \Theta, \eta] = P[D|M, \Theta] \times P[M|\eta] \times P[\Theta] \times P[\eta] \ . \tag{4.2}$$

Using Bayes theorem, we note that the RHS is proportional to $P\left[M,\eta,\Theta|D\right]$, so we may run Bayesian inferences on the model M, and parameters η and Θ through

$$P[M, \Theta, \eta|D] \propto P[D|M, \Theta] \times P[M|\eta] \times P[\Theta] \times P[\eta] \ . \tag{4.3}$$

4.2 Application to steady-state SPEL

A Bayesian hierarchical model framework specified for erosional processes described by SPEL must account for data on channel relief, dz/dx, and discharge, Q. Recall that the model describing the physical process is given by

$$\frac{dz}{dx} = \left(\frac{U}{K}\right)^{1/n} Q(x)^{-m/n} \ . \tag{4.4}$$

Taking the log of both sides so that the dimensionless exponents become multiplicative constants, which simplifies the equation for computational modeling purposes, we have

$$\log \frac{dz}{dx} = \frac{1}{n} \log \frac{U}{K} - \frac{m}{n} \log Q \ . \tag{4.5}$$

Specifically, the log transformations keep the model from computing unreasonably large numbers that often result in approximations of infinity. The slope observations $y^* = dz/dx$ may readily be transformed into log-space by $y = \log(y^*)$. The transformation for measured Q values is identical. There is never an issue with the singularity caused by $\log(0)$, because the minimum value for measured slopes in the region are $\mathcal{O}(10^{-2})$ and discharge rates are strictly positive. We limit the constants m and n to physically-relevant values. We will use different values for m and n in the model that have been determined to correspond to different geomorphological behaviors (e.g., Montgomery, 1994; Tucker and Bras, 2000). For simplicity, we define $\phi = \log(U/K)$ and $D = \log(Q)$. The previous equation is now,

$$y = \frac{1}{n}\phi - \frac{m}{n}D \ . \tag{4.6}$$

In the following subsections, we will discuss how to specify (4.6) within the three main components of a hierarchical Bayesian framework: the data, prior process, and prior parameter models.

4.2.1 Data model

An important consideration made in this manuscript is that we are operating over long geologic time scales, for which the steady-state assumption for erosion and uplift processes holds. Additionally, by using distinct elevation classes determined through landscape self-organization, we are purposefully charactering the landscape based on elevation regimes, which lack any direct spatial dependence for y, say at a given distance x, as seen in the original configuration of the steady-state SPEL (4.4). The data model for y will be represented by the RHS of (4.6) plus some measurement error e_y

$$y = \frac{1}{n}\phi - \frac{m}{n}D + e_y \ , \quad e_y \sim \text{Normal}\left(0, \sigma^2\right) \ . \tag{4.7}$$

where $e_y \sim \mathrm{N}(0, \sigma^2)$ and expresses error in the measurement of the data. The data, y, will be considered normally distributed and centered on the output from the RHS of (4.6), which we will refer to as the process model M, i.e.

$$y|M, \sigma^2 \sim \text{Normal}\left(M, \sigma^2\right) \ . \tag{4.8}$$

4.2.2 Prior process model

The process model is based on SPEL, and specifically on the relationship that channel slope is proportional to discharge, Q, up to a constant, U/K. We specify the *true* process as the RHS of (4.6)

$$M_0 = \frac{1}{n}\phi - \frac{m}{n}D \ . \tag{4.9}$$

As all other values in the true process (4.9) are constants, the prior process model will be conditional on the physical parameter ϕ. The prior process model will be centered on the true process (4.9) with some error, e_M, that accounts for the fact that (4.9) is not a perfect descriptor of the physical process at hand

$$M = M_0 + e_M \ , \quad e_M \sim \text{Normal}\left(0, \tau^2\right) \ . \tag{4.10}$$

Thus, the process model is normally distributed around its *true* value

$$M|\phi, \tau^2 \sim \text{Normal}\left(M_0, \tau^2\right) \ . \tag{4.11}$$

It is important to note a physical constraint on the range of slopes that occur in the region. Based on the data collected, the slopes will fall between 10^{-3} and 1. Thus, we restrict the prior process model to the domain $R \in [\log(10^{-3}), 0]$. The prior process is now a truncated normal distribution given by

$$M|\phi, \tau^2 \sim \text{Normal}_R\left(M_0, \tau^2\right) \ , \quad R \in \left[\log\left(10^{-3}\right), 0\right] \ . \tag{4.12}$$

4.2.3 Prior on parameters

Three parameters require prior specification in the physical-statistical model: 1) the log of the ratio of uplift to erosion, ϕ; 2) the variance term associated with measurement error from the data model, σ^2; and 3) the variance term associated with error from the physical model, τ^2. We place an informative prior on U/K based on values commonly found in the literature. Typical values are $U = 2$ mm/yr and $K = 4\times10^{-11}\text{m}^{1-3m}\text{s}^{m-1}$, where the units of K depend on the dimensionless exponent m (Wu et al., 2006; Roe et al., 2003, 2002). Thus, when $m = 1/3$, the dimensions of K are $\text{s}^{-2/3}$, and under this circumstance a common value for the uplift ratio is $U/K = 500.7\text{m yr}^{-1/3}$. Gamma distributions are typical for physical parameters in hydrology, so we choose a Gamma prior centered on $\log(500.7) = 6.22$. To ensure semi-conjugacy, we choose Gamma priors for both $1/\sigma^2$ and $1/\tau^2$ with shape and scale parameters of 2 and 6. The prior specification for the physical-statistical model is then

$$\phi \sim \text{Ga}\,(a, b) \tag{4.13}$$

$$1/\sigma^2 \sim \text{Ga}\,(c, d) \tag{4.14}$$

$$1/\tau^2 \sim \text{Ga}\,(f, g)\ , \tag{4.15}$$

where $a = 6.22$, $b = 1$, $c = f = 2$ and $d = g = 6$.

4.3 Physical-statistical model specifications

Using the model specifications provided in the previous section, we find the joint conditional distribution for the data, process, and parameters of the physical-statistical

model is given by

$$
\begin{aligned}
p(\phi, M, 1/\sigma^2, 1/\tau^2|y) &\propto p(y|M, \sigma^2)\ p(M|\phi, \tau^2)\ p(\phi)\ p(1/\sigma^2)\ p(1/\tau^2) \\
&= \frac{1}{\sqrt{2\pi\sigma^2}} \exp\left[\frac{-1}{2\sigma^2}\left(y - M\right)^2\right] \\
&\times \left(\frac{\mathbf{1}\left(M \in R\right)}{F\left[0\right] - F\left[\log\left(10^{-3}\right)\right]}\right) \frac{1}{\sqrt{2\pi\tau^2}} \exp\left[\frac{-1}{2\tau^2}\left(M - M_0\right)^2\right] \\
&\times \phi^{a-1} \exp\left[-b\phi\right] \left(\frac{1}{\sigma^2}\right)^{c-1} \exp\left[-\frac{d}{\sigma^2}\right] \left(\frac{1}{\tau^2}\right)^{f-1} \exp\left[-\frac{g}{\tau^2}\right] \ ,
\end{aligned}
\tag{4.16}
$$

where F indicates the normal cumulative distribution function (CDF) and $\mathbf{1}(...)$ is an indicator function that equals 1 if what lies within the parentheses is true and 0 otherwise. From this joint conditional distribution, the full conditional distributions are derived. The model parameters are sampled from these distributions. Full conditional distributions allow for iterative sampling using basic Markov chain Monte Carlo (MCMC) techniques. They are determined for each parameter by considering only the terms in the joint conditional distribution (4.16) which depend on that particular parameter. Complete derivations of each full conditional distribution are shown in Appendix A. It is rather straightforward to see that the full conditional distributions for M, $1/\sigma^2$, and $1/\tau^2$ will be semi-conjugate, the sampling distribution for M conditional on all other model parameters will be a Normal distribution and those for $1/\sigma^2$, and $1/\tau^2$ will be Gamma distributions. The full conditional distribution of ϕ, however, does not simplify further into a conjugate form, so we must employ a Metropolis-Hastings sampling method for this distribution. Metropolis-Hastings sampling involves stochastically sampling from a symmetric distribution and accepting a given sample with a probability that depends on the ratio of the target distribution, the non-standard distribution that is difficult to sample from. A step-by-step procedure for this technique is provided in the following section. A

table of inputs as well as thorough explanations for how the inputs were determined may be found in Appendix B.

4.4 Sampling procedure

We rely on MCMC to sample from the full conditional distributions of the parameters and to run the posterior inferences on ϕ to estimate uplift rates. Here we present the forms of these distributions:

$$p(M|-) \propto \mathrm{N}_R\left(\mu_n, \tau_n\right) \ , \quad R \in \left[\log\left(10^{-3}\right), 0\right] \tag{4.17}$$

$$\mu_n = \frac{y/\sigma^2 + M_0/\tau^2}{1/\sigma^2 + 1/\tau^2}$$

$$\tau_n = \frac{1}{1/\sigma^2 + 1/\tau^2}$$

$$p(\phi|-) \propto \phi^{a-1} \exp\left[-\frac{\phi^2}{2\tau^2} - \phi\left(b - \frac{D}{\tau^2} - \frac{M}{\tau^2}\right)\right] \tag{4.18}$$

$$p(1/\sigma^2|-) \propto \mathrm{Ga}(c_n, d_n) \tag{4.19}$$

$$c_n = c + \frac{1}{2}$$

$$d_n = \frac{(y-M)^2}{2} + d$$

$$p(1/\tau^2|-) \propto \mathrm{Ga}(f_n, g_n) \tag{4.20}$$

$$f_n = f + \frac{1}{2}$$

$$g_n = \frac{(M-M_0)^2}{2} + g$$

Complete derivations of these distributions are contained in Appendix B. Note that the parameter of interest in regards to estimating uplift, ϕ, does not have a standard form for its full conditional distribution, so we use Metropolis-Hastings to sample from its target distribution. Our procedure consists of the following steps:

1. Specify physical model parameters and hyperparameters for priors.

2. Set initial values for M, ϕ, σ^2 and τ^2.

3. Set tuning parameter, k, the standard deviation of the normal jumping distribution for the Metropolis-Hastings algorithm.

4. Consider large T and do the following for $t = \{1, ..., T\}$.

4.a. Sample $\sigma^{2(t)}$ from its full conditional with all other parameters fixed.

4.b. Sample $\tau^{2(t)}$ from its full conditional with all other parameters fixed.

4.c. Sample $M^{(t)}$ from its full conditional with all other parameters fixed.

4.d. Sample a candidate value for ϕ, ϕ^*, from a Normal jumping distribution.

4.e. Calculate the acceptance ratio using the target distribution for ϕ:

$$r = \frac{\phi^{*(a-1)} \exp\left[-\frac{\phi^{*2}}{2\tau^{2(t)}} - \phi^* \left(b - \frac{D}{\tau^{2(t)}} - \frac{M}{\tau^{2(t)}}\right)\right]}{\phi^{(t-1)(a-1)} \exp\left[-\frac{\phi^{(t-1)2}}{2\tau^{2(t)}} - \phi^{(t-1)} \left(b - \frac{D}{\tau^{2(t)}} - \frac{M}{\tau^{2(t)}}\right)\right]}$$

4.f. Set $\phi^{(t)} = \phi^*$ with the probability $p = \min(1, r)$, else set $\phi^{(t)} = \phi^{(t-1)}$.

We use a large number of simulations $T = 2 \times 10^4$, but occasionally the acceptance ratio yields 'not a number' due to one or more of the terms converging to infinity. Once these instances are removed, the effective simulation size is around $T_{\text{eff}} = 1.98 \times 10^4$. Mixing is not ideal in these samples, as seen in the sample autocorrelation plots in Appendix C, so we thin by taking one in every four samples. Mixing, and autocorrelation, improves substantially by thinning (see Appendix C). We perform inferences on the MCMC samples after a burn-in period of 1000 samples, which corresponds to discarding 4000 samples before thinning. The sample size after

thinning and burn-in is around 4000. Trace plots for each parameter before and after thinning are displayed in Appendix D.

Since we are concerned with estimating a single parameter, ϕ, with Metropolis-Hastings, the tuning parameter, k, must be set so that we are accepting the sampled values of ϕ about half of the time. This tuning parameter in a sense restricts how far away the next sampled value of ϕ will be from its current value. To ensure $\sim$50% acceptance rate, we must choose different values for the tuning parameter, k, depending on the choice of m and n used in the model. For $m = 1/3$ and $n = 2/3$, the value is $k = 2$; for $m = 1/2$ and $n = 1$, the value is $k = 3$; and for $m = n = 1$, the value is $k = 5$.

In this chapter we undertook the development of a physically-based statistical model that is used to estimate uplift rates at the elevation class scale for the six basins in the study area. These uplift rates provide a means to make quantitative comparisons of the geomorphological process that are occurring within these basins. The following chapter provides the results from the model developed here and a discussion of how they compare with hypotheses suggested by the preliminary data analysis.

5

Estimated Uplift in the Central Andes and Geomorphologic Implications

Thus far, we have provided suggestive evidence of interactions between precipitation and topography in the central Andes. The goal of this chapter is to offer quantitative support by estimating uplift rates using the physical-statistical model developed in Chapter 4. We capture the qualitative links between climate and landscape evolution through the parameterization of the model. Specifically, we found similarities between how first order outlets and precipitation features were distributed by elevation within each of the six watersheds in the study area. We incorporate this effect by specifying slope in SPEL (4.4) using the maximum first order stream relief over the maximum first order stream length for each elevation class. This choice incorporates two of the main hypotheses of this manuscript: 1) the elevation classes provide a natural scale to evaluate geomorphic processes; and 2) the link between first order streams and precipitation events are a first-order effect on landscape evolution in the study region. Additionally, the effects of climate are incorporated directly by parameterizing the discharge term using MAP estimated from the TRMM satellite

data. We consider both the unadjusted and adjusted estimates determined using MAP from the Kospiñata rain gauge network located in the Madre de Dios basin (see Chapter 2). Besides providing the results of the physical-statistical model, comparisons are made between the model results and preliminary analyses concerning hypsometry conducted in Chapter 2. Previously measured values from the literature on uplift in the Andes are also considered. Finally, since the physical-statistical model is highly parameterized based on the central Andes data, we discuss the possible model sensitivities to the choices made. In all, this chapter provides a robust discussion of the results from both the physically-based statistical model and the prior data analysis conducted in Chapters 2 and 3.

The physical-statistical model developed in Chapter 4 is employed to estimate ϕ for each elevation class of the six watersheds in the central Andes study region using different values of the dimensionless exponents m and n. The results from the model displayed in Table 5.1 use the MAP derived from the TRMM 3B42 v.7 product and those in Table 5.2 correspond to the orographic adjustment made using the Kospiñata rain gauge network data as a reference. In both tables, we show the model outputs determined using the value of m and n for which the estimated slope best matches the characteristic slope (i.e. model input) for all of the elevation classes. Each choice of m and n comes with its own assumption about how erosion behaves (Montgomery, 1994; Tucker and Bras, 2000):

1. $m = 1/3, n = 2/3$: Erosion rate depends on unit stream power
2. $m = 1/2, n = 1$: Erosion proportional to excess shear stress
3. $m = 1, n = 1$: Erosion proportional to stream power

Tables 5.1 and 5.2, provide the expected value for ϕ, the expectation and 90% interval for the constant uplift rate, U, given the fixed K-value specified in the prior, and

the estimated and characteristic slope values.

5.1 Comparisons with prior data analysis

In order to interpret which values of m and n yield the best results, we find the expected value for estimated slope (i.e. $\exp(M)$) and compare it to the characteristic slopes for each elevation class. The value of m and n that produces estimated slopes for each elevation class that consistently match the model input slopes are then selected to provide the ϕ and uplift results in Tables 5.1 and 5.2. It falls out immediately that the optimum values of m and n determined by comparing slopes match hypotheses garnered from our initial data analysis. Table 5.3 summarizes the hypotheses along with the values of m and n selected by the physical-statistical model. Based solely on basin hypsometry, we concluded that the Huallaga, Madre de Dios and Salar de Uyuni are heavily under the influence of fluvial erosion, the Ucayali is predominantly undergoing tectonic uplift, and Marañón and Beni are within a balance of fluvial erosion and tectonic uplift. Our results suggest that, under modest MAP estimates (see Table 5.1), erosion is proportional to stream power in the Huallaga, Ucayali, Madre de Dios and Salar de Uyuni, and thus fluvial erosion is the dominant process. Additionally, under the same MAP estimates, the Marañón and Beni are undergoing erosion that is proportional to excess shear stress. Later, with the orographically-adjusted MAP (see Table 5.2), we see find the same results for the Marañón, Huallaga, Madre de Dios and Beni as before, but Ucayali is now best represented by $m = 1/2$ and $n = 1$ (and, recall, an orographically-adjusted MAP is not considered for the Salar du Uyuni).

Table 5.1 Results of physical-statistical model using MAP derived from TRMM 3B42.

Basin	**EC**	**Mean ϕ**	**Est. U[a] $\left(\frac{\text{mm}}{\text{yr}}\right)$**	**90% int. U**	**Est. $\frac{dz}{dx}$**	$\frac{dz}{dx}$
Marañón[b]	1	7.73	4.22	$(0.02, 16.85)$	0.08	0.06
	2	7.84	4.84	$(0.02, 17.70)$	0.09	0.10
	3	7.48	3.16	$(0.02, 10.58)$	0.07	0.05
	4	7.60	3.48	$(0.02, 13.11)$	0.10	0.10
Huallaga[c]	1	11.96	9.00	$(0, 35.72)$	0.03	0.02
	2	12.03	8.87	$(0, 32.43)$	0.04	0.04
	3	11.99	6.00	$(0, 28.91)$	0.04	0.03
	4	12.09	6.45	$(0, 24.94)$	0.04	0.04
	5	12.28	3.42	$(0, 20.01)$	0.04	0.04
Ucayali[c]	1	11.83	8.03	$(0, 24.69)$	0.03	0.03
	2	11.86	10.57	$(0, 25.19)$	0.06	0.06
	3	11.97	7.25	$(0, 20.12)$	0.05	0.04
	4	11.84	9.20	$(0, 18.65)$	0.08	0.11
	5	12.18	3.32	$(0, 9.13)$	0.06	0.07
Madre de Dios[c]	1	12.18	2.31	$(0, 8.88)$	0.07	0.07
	2	12.31	1.93	$(0, 5.24)$	0.04	0.04
	3	12.30	1.89	$(0, 5.84)$	0.06	0.06
	4	12.30	1.12	$(0, 3.86)$	0.04	0.04
	5	12.28	0.68	$(0, 2.23)$	0.02	0.03
Salar de Uyuni[c]	1	12.33	3.48	$(0, 11.43)$	0.03	0.02
	2	12.12	2.84	$(0, 7.99)$	0.02	0.02
	3	12.27	2.13	$(0, 5.89)$	0.02	0.01
	4	12.34	1.68	$(0, 5.11)$	0.02	0.01
Beni[b]	1	7.81	4.20	$(0.02, 15.93)$	0.09	0.09
	2	7.64	4.20	$(0.02, 14.06)$	0.07	0.06
	3	7.87	4.24	$(0.02, 16.18)$	0.11	0.12
	4	7.68	3.89	$(0.02, 15.04)$	0.09	0.09
	5	7.60	3.44	$(0.02, 11.53)$	0.11	0.11
	6	7.61	3.00	$(0.02, 12.18)$	0.12	0.12
	7	7.50	3.11	$(0.02, 11.68)$	0.12	0.12
	8	6.90	1.33	$(0.01, 5.28)$	0.10	0.07

[a] Estimated U determined from posterior samples of ϕ using $K = 4 \times 10^{-11} \frac{\text{m}^{(1-3m)}}{\text{s}^{(1-m)}}$.

[b] $m = 1/2$, $n = 1$

[c] $m = 1$, $n = 1$

Table 5.2 Results of physical-statistical model using rain gauge adjusted MAP.

Basin	**EC**	**Mean ϕ**	**Est. U[a] $\left(\frac{\text{mm}}{\text{yr}}\right)$**	**90% int. U**	**Est. $\frac{dz}{dx}$**	$\frac{dz}{dx}$
Marañón[b]	1	8.10	6.65	$(0.02, 23.36)$	0.07	0.06
	2	8.23	7.93	$(0.03, 29.25)$	0.09	0.10
	3	7.85	4.31	$(0.02, 17.22)$	0.07	0.05
	4	7.93	5.39	$(0.02, 17.60)$	0.10	0.10
Huallaga[c]	1	11.68	11.01	$(0, 35.72)$	0.04	0.02
	2	11.73	11.59	$(0, 32.43)$	0.05	0.04
	3	11.83	9.72	$(0, 28.91)$	0.04	0.03
	4	11.85	11.47	$(0, 24.94)$	0.05	0.04
	5	11.99	8.03	$(0, 20.01)$	0.04	0.04
Ucayali[b]	1	8.03	4.05	$(0.02, 21.38)$	0.04	0.03
	2	8.25	5.13	$(0.03, 29.22)$	0.06	0.06
	3	7.95	4.13	$(0.02, 19.34)$	0.05	0.04
	4	8.23	6.04	$(0.03, 27.73)$	0.10	0.11
	5	7.81	4.88	$(0.02, 16.83)$	0.08	0.07
Madre de Dios[c]	1	12.12	4.75	$(0, 14.93)$	0.07	0.07
	2	12.14	2.36	$(0, 8.33)$	0.04	0.04
	3	12.19	3.33	$(0, 9.01)$	0.06	0.06
	4	12.32	1.75	$(0, 5.07)$	0.04	0.04
	5	12.28	0.81	$(0, 2.51)$	0.02	0.03
Beni[b]	1	8.14	6.76	$(0.03, 25.16)$	0.09	0.09
	2	7.98	4.97	$(0.02, 19.72)$	0.06	0.06
	3	8.25	7.64	$(0.03, 30.32)$	0.10	0.12
	4	7.98	5.51	$(0.02, 19.88)$	0.09	0.09
	5	7.82	4.30	$(0.02, 15.46)$	0.10	0.11
	6	7.81	4.24	$(0.02, 15.75)$	0.11	0.12
	7	7.69	3.55	$(0.02, 13.84)$	0.11	0.12
	8	7.08	1.64	$(0.01, 6.49)$	0.10	0.07

[a]Estimated U determined from posterior samples of ϕ using $K = 4 \times 10^{-11} \frac{\text{m}^{(1-3m)}}{\text{s}^{(1-m)}}$.

[b]$m = 1/2$, $n = 1$

[c]$m = 1$, $n = 1$

Table 5.3 Comparison of previous data analysis to model results.

Data Analysis Method	**Marañón**	**Huallaga**	**Ucayali**	**Madre de Dios**	**Salar de Uyuni**	**Beni**
Hypsometric Integral						
Young/Inequilibrium				X		
Transitional	X					X
Equilibrium		X	X		X	
Hypsometric Curvature						
Erosion		X		X	X	
Uplift			X			
Balanced	X					X
Cross Correlation						
Tectonics	X		X			X
Climate		X		X	X	
Physical-statistical Model						
Unadjusted MAP						
$m = 1/2, n = 1$[a]	X					X
$m = n = 1$[b]		X	X	X	X	
Adjusted MAP						
$m = 1/2, n = 1$[a]	X		X		–	X
$m = n = 1$[b]		X		X	–	

[a]Erosion proportional to excess shear stress.

[b]Erosion proportional to stream power.

Additional early results from the preliminary data analysis were determined from cross-correlations between the distributions of first order outlets and TRMM PFs binned by elevation. From these results, we claimed that climate has smaller effect in the Marañón, Ucayali and Beni basins, and a larger effect in the Huallaga, Madre de Dios and Salar de Uyuni. From Table 5.3, it is evident that the model results with the unadjusted and adjusted MAP inputs generally agree with the findings from the cross-correlations when taking into account the values of m and n determined as the best fit. The only exceptions are the Ucayali basin exhibiting different behavior with unadjusted MAP, the Madre de Dios basin having a much higher hypsometric integral, and the fact that results for the Salar de Uyuni were not computed for the adjusted MAP. Otherwise, the basins found to have tectonics as the dominant process also have $m = 1/2$ and $n = 1$ as the best fit values for these parameters, or in other words yield optimal results under the assumption that erosion is proportional to excess shear stress. Conversely, those with climate as the governing process find $m = 1$ and $n = 1$, or erosion is proportional to stream power is the underlying assumption. It is prudent to note that the dimensionless exponents choice of $m = 2/3$ and $n = 1/3$ never result in the best agreement between slope values for any of the basins, suggesting that within the central Andes region considered in this manuscript, the assumption that erosion rate depends on unit stream power is inconsistent with the steady-state SPEL model.

Overall, in Table 5.3, across the previous data analysis methods and the model results we find similar behavior for the Marañón and Beni, and the Huallaga, Madre de Dios and Salar de Uyuni. The Ucayali appears to have qualitatively and quantitatively different behavior from the other basins. We found agreement between the results of the physical-statistical model, hypsometric analysis, and cross-correlations between first order outlet and TRMM PF distributions. This general consistency suggests the six basins are undergoing three distinct geomorphologic processes under

which the Huallaga, Madre de Dios and Salar de Uyuni are similar, the Marañón and Beni are grouped together, and the Ucayali makes up its own category. The Huallaga, Madre de Dios, and Salar de Uyuni are controlled by climate-driven fluvial processes. No single governing process emerges in the Marañón and Beni basins, but evidence suggests a balance between erosion and uplift where climate is less of a contributing factor than tectontics. The Ucayali appears to be in a state of equilibrium where tectonic uplift is the key driver of landscape evolution, but fluvial erosion may also have a significant role.

5.2 Comparisons with basin hypsometry

There is strong agreement between the hypsometry for each elevation class and the estimated uplift, U, for the values of m and n where estimated slope best matches the true slope. Figures 5.1, 5.2, and 5.3 show the estimated uplift rates for the unadjusted and adjusted TRMM MAP for each watershed along with its corresponding hypsometric curve and elevation profiles. The basins in Figure 5.1 are those located in the northern region of the study, while those in Figure 5.2 are located in the central region and the last two shown in Figure 5.3 are found in the southern region. A noticeable feature is that both estimated uplift rates reflect the qualitative behavior of basin hypsometry. Convexity in the hypsometric curve associates with higher effective uplift, while concave sections along the curve reflect lower rates of uplift. For example, in Figure 5.1a, the most convex sections are in the first and second elevation classes and these classes serve as the locations of the highest effective uplift rates in Figure 5.1b for both MAP values. The ability for the physical-statistical model to capture the qualitative hypsometric behavior demonstrates its strength as a method to estimate key parameters of SPEL. Additionally, the adaptation of a natural scale – the elevation class – allows for the estimation of uplift in geomorphologically similar regions within a basin. We reiterate that the elevation classes were determined

based on basin self-organization and were found to mark areas of distinct curvature along the hypsometric curves (see Figure 2.4). Further using characteristic physical properties of the elevation classes allowed for computation of uplift rates that reflect the hypsometric behavior.

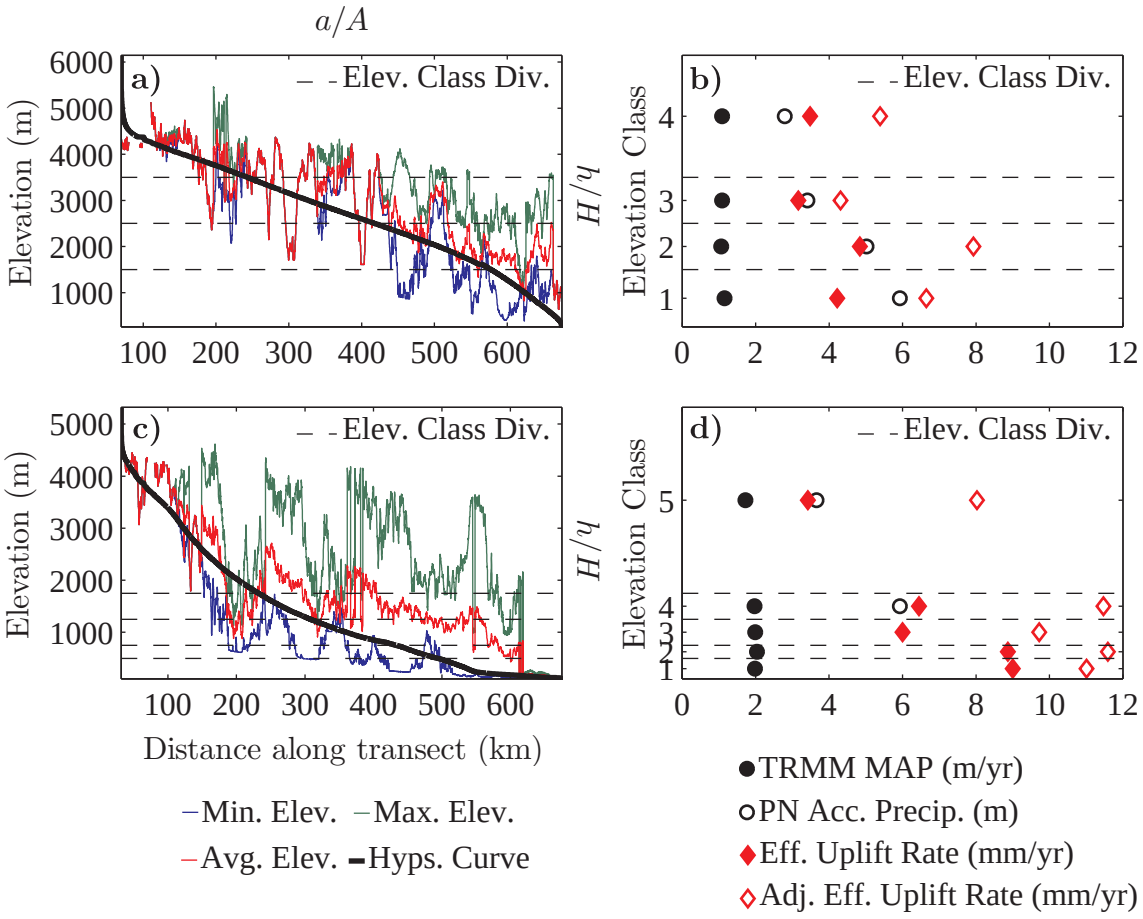

FIGURE 5.1 Plots on the left-hand side of the page show minimum, maximum, and average elevation profiles along a basin-wide transect that runs south to north. The hypsometric curve is plotted over the elevation profiles. The plots on the right-hand side of the page show MAP estimated from the TRMM 3B42 v.7 product and the mean precipitation depth for the Peru rain gauges plotted by elevation class. Note the severe underestimation of MAP by TRMM. The Kospiñata network is used here as a means to assess the impact of rainfall uncertainty, specifically the underestimation of orographic rainfall in mountainous regions (Barros, 2013). The estimated effective uplift rates using the TRMM MAP and the orographically-adjusted MAP are also displayed. a-b) Marañón. c-d) Huallaga.

The ability for the model results to match hypsometry under the simple parametrization strategy employed in this manuscript is paramount. An obvious feature of

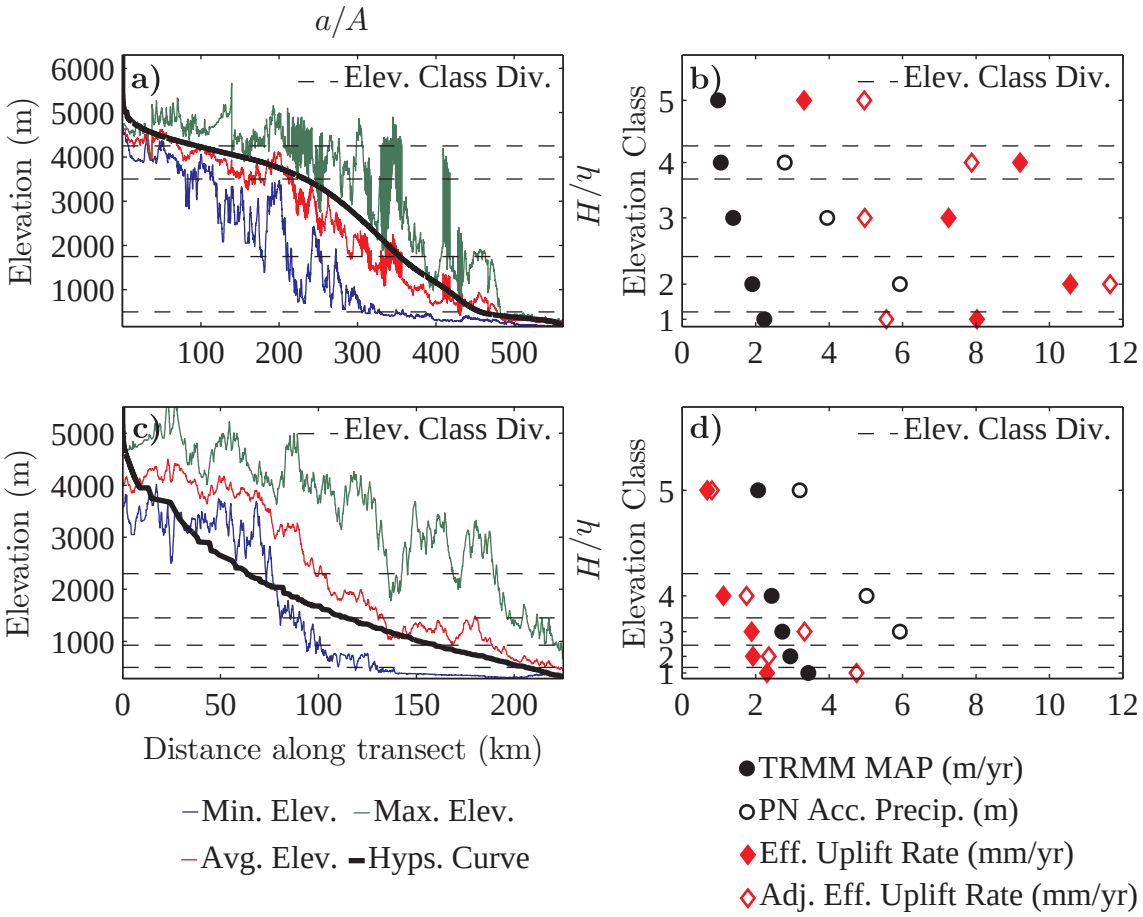

FIGURE 5.2 Plots on the left-hand side of the page show minimum, maximum, and average elevation profiles along a basin-wide transect that runs south to north. The hypsometric curve is plotted over the elevation profiles. The plots on the right-hand side of the page show MAP estimated from the TRMM 3B42 v.7 product and the mean precipitation depth for the Peru rain gauges plotted by elevation class. The Kospiñata network is used here as a means to assess the impact of rainfall uncertainty, specifically the underestimation of orographic rainfall in mountainous regions (Barros, 2013). The estimated effective uplift rates using the TRMM MAP and the orographically-adjusted MAP are also displayed. a-b) Ucayali. c-d) Madre de Dios.

steady-state SPEL, particularly by considering discharge to be a precipitation-weighted area, is that as precipitation increases, uplift will increase if all other parameters are held constant. Undoubtedly, since the discharge term considered here is cumulative, the lower elevation classes always have higher discharge inputs than the class above it. However, by constraining the slopes to characteristic values governed by the elevation classes, the model results obtained do not simply increase as a function of

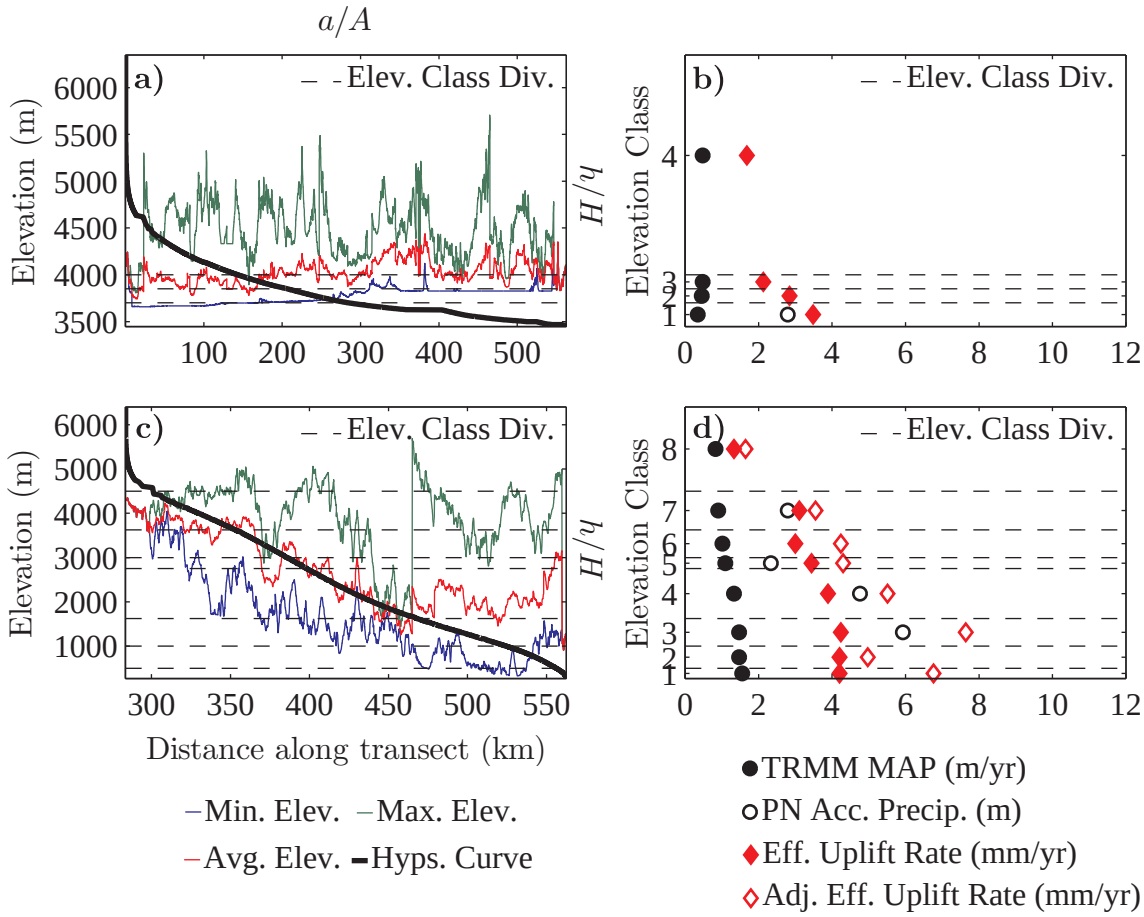

FIGURE 5.3 Plots on the left-hand side of the page show minimum, maximum, and average elevation profiles along a basin-wide transect that runs south to north. The hypsometric curve is plotted over the elevation profiles. The plots on the right-hand side of the page show MAP estimated from the TRMM 3B42 v.7 product and the mean precipitation depth for the Peru rain gauges plotted by elevation class. The Kospiñata network is used here as a means to assess the impact of rainfall uncertainty, specifically the underestimation of orographic rainfall in mountainous regions (Barros, 2013). The estimated effective uplift rates using the TRMM MAP and the orographically-adjusted MAP are also displayed. a-b) Salar de Uyuni. c-d) Beni.

decreasing elevation class. For example, in Figure 5.2a the hypsometric curve for the Ucayali basin shows highly concave regions in the 5th, 3rd, and 1st elevation classes. As such, these elevation classes exhibit the lowest uplift rates (Figure 5.2b). The cumulative discharge considered for the first elevation class is an order of magnitude larger than that computed for the fourth elevation class (see Table B.1), and yet due to the constraint we place on the slope, the effective uplift rates match basin

hypsometry.

5.3 Comparisons with previously measured uplift values

In Appendix F, we provide uplift and erosion rates given in the literature. The highest uplift rate reported in the present manuscript is 11.49 mm/yr, which is slightly higher than the highest value in the literature of 10 mm/yr, but also barely outside of the error range. Thus, the physical-statistical model at least yields uplift estimations that are of the same order of magnitude of those measured in previous studies. However, directly comparing the magnitude of the uplift rates reported here to those in Table F.1 is limited by the fact that all previous measurements are dependent on a particular geologic time period and at spatial scales that are either point-wise or much larger than the elevation classes considered at present. Further, many of these estimates are inconsistent with the assumption of uplift balanced by erosion during a particular period of time. The steady-state form of SPEL requires that we consider a period much longer than those used by the authors cited in Table F.1.

5.4 Spatial trends in average basin uplift

By taking the average of the uplift rates computed for each elevation class within a basin, we can determine an average uplift rate for the entire basin. In Figure 5.4, the average uplift rates computed using the unadjusted and adjusted MAP are shown. These average rates are higher in the Marañón, Huallaga, and Ucayali, and lower in the Madre de Dios, Salar de Uyuni, and Beni. This spatial trend may be related to the tectonic forcing imposed by the subducting Nazca plate. Figure 5.5 shows the location of converging Nazca and South American plates along with contours indicating depth to the subducting Nazca plate. The Marañon and Huallaga basins are within a region of shallow subduction with lower shear stress, thus very little of the total uplift for these basins is attributable to tectonic uplift. The Madre de Dios,

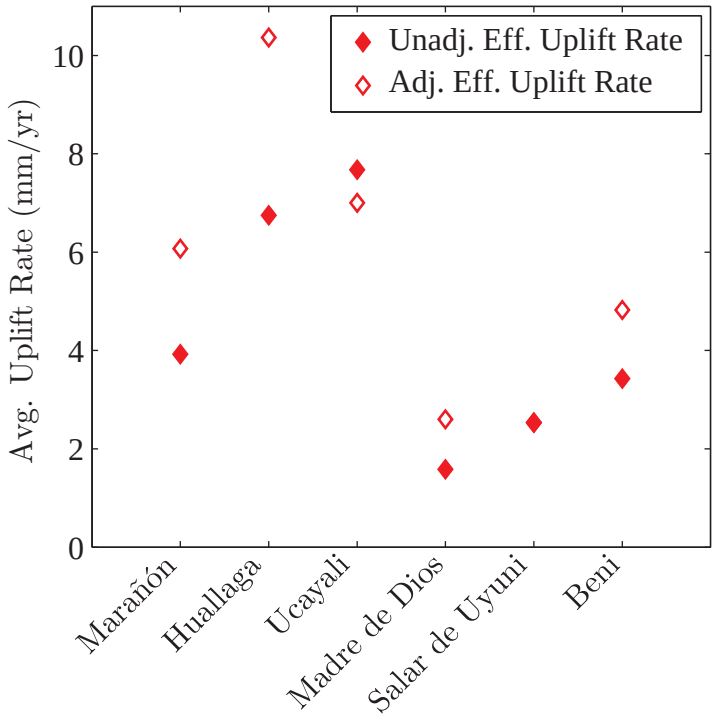

FIGURE 5.4 Average uplift rates for each of the six basins in the study area using the estimated uplift rates for each elevation class. The averages are shown for uplift computed using both unadjusted and adjusted MAP values. Note how the basins with higher average uplift rates are closer in depth to the subducting Nazca plate shown in Figure 5.5.

Salar de Uyuni and Beni basins are located in regions of steep subduction. Thus, much of the total uplift for these three basins results from tectonic uplift. It is reasonable, then, that the effective uplift rates computed from the physical-statistical model are lower for the Marañón and Huallaga and higher for the Madre de Dios, Salar de Uyuni and Beni – the effective uplift serves as a proxy for surface uplift. Since uplift in the northern basins is predominantly surface uplift, the average effective uplift rates for these basin are higher, while uplift in the Madre de Dios, Salar de Uyuni and Beni basins is mostly tectonically driven and thus the effective uplift rates here are lower. The Ucayali basin has a mix of shallow and steep subduction, with the steepest subduction occurring in the lowest elevations for this basin (see Figure 5.5). Thus, for this basin, different regions of each elevation class are experi-

encing variability in magnitude of shear stress due to subduction, which explains in part why the physical-statistical model could not determine a single case of m and n that best summarized the underlying assumption regarding erodibility behavior for this basin.

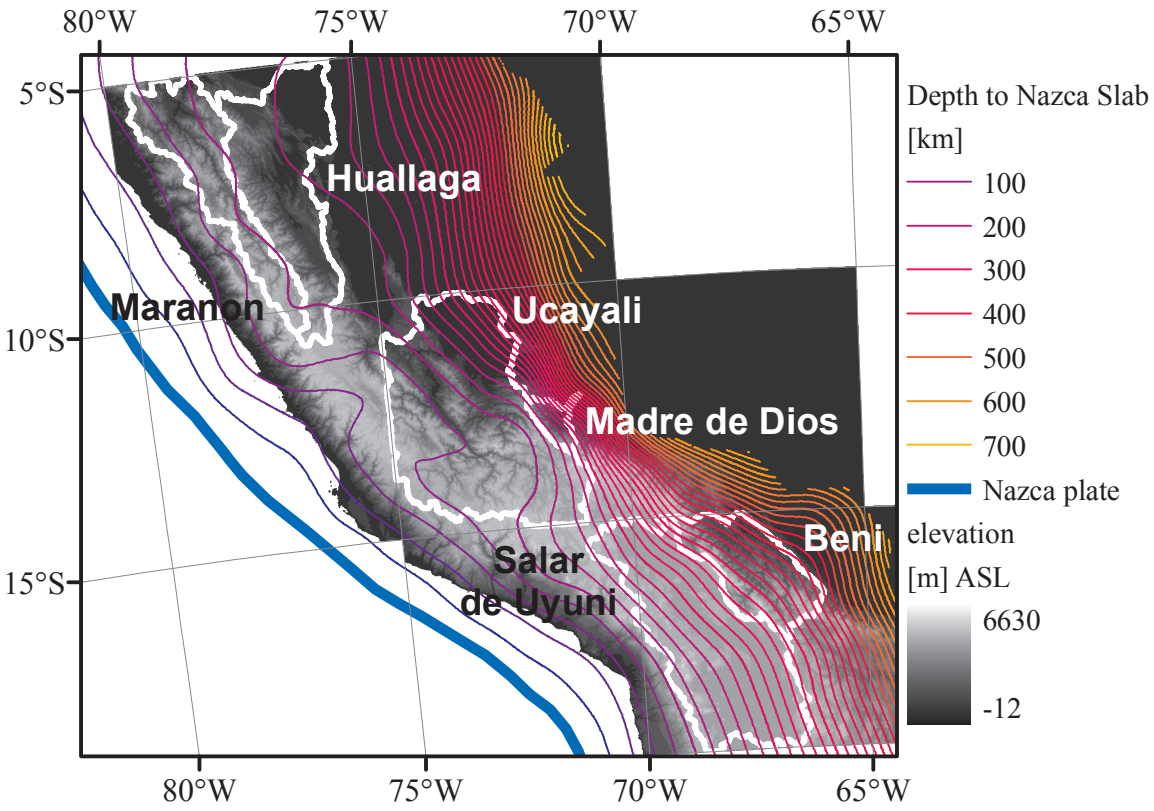

FIGURE 5.5 Map of basins with contours representing depth to subducting Nazca slab. Data on the location and depth of slab provided by USGS.

5.5 Sensitivity to parameter selection

In this manuscript, we made a series of parameter choices that had a direct effect on the estimated effective uplift rates shown in Tables 5.1 and 5.2. First, the choice of a prior for ϕ centered on $U = 2$ mm/yr and $K = 4 \times 10^{-11}\text{m}^{1-3m}\text{s}^{m-1}$, had an effect on the outcome of this term. Choice of an informative prior has a tendency to

shrink results closer to the mean of the prior distribution in a Bayesian hierarchical model; however, using an informative prior is important to ensure meaningful results in Bayesian statistics (Efron, 2013). An alternative is to run the physical-statistical model with a prior centered on values of U and K taken from previous literature that uses different configurations of SPEL (e.g. Hilley and Strecker, 2004; Hilley et al., 2004), which estimate values for K, m, and n by approximating the underlying geologic structure with a simplified Coulomb wedge model.

There is a clear effect on choice of m and n which was explored in this manuscript. Here, we find justification to report results for the m and n values where the estimated slope best matches the characteristic slope. We demonstrated that this approach provides strong agreement with both hypsometry and the results from cross-correlations between the distributions of first order outlets and precipitation events. A more formal method to determine optimal m and n values, however, is to iteratively try different values for each exponent to determine best fit, but this exercise is not the objective of the present paper.

Another parameter changed in the model is the MAP – we used a value from the TRMM 3B42 v.7 product and an orographic adjustment to this product using Kospiñata rain gauge data. The general effect of using the orographically-adjusted MAP is a change in the magnitude for each elevation class, but not in the behavior, which always matches the hypsometry. In general, using the orographically-adjusted MAP results in an increase in the estimated effective uplift values. This occurs in all basins except for the Ucayali, which can be explained by the difference in m and n values used to obtain the results.

6

Conclusion

The main result of this thesis is the demonstration of a comprehensive, novel method for exploring the role of regional climate in orogenic development. This task was accomplished by first characterizing basins using hypsometry and then distinguishing basins by elevation class, a measure of basin self-organization. Initial inspection within the study area resulted in the observation of similar geomorphologic behavior in certain basins. The Marañón and Beni exhibit an apparent balance between uplift and erosion. The Huallaga, Madre de Dios and Salar de Uyuni demonstrated fluvial erosion dominated dynamics, while the Ucayali exhibited qualitatively different behaviors from the other basins. We then classified regional climate by evaluating the organization of precipitation and found a unique relationship in the persistent similarities between the distributions of first order outlets and precipitation events. This link was hypothesized to provide an important constraint on geomorphologic behavior. To study this qualitative observation more rigorously, a physically-based Bayesian hierarchical model was developed. By specifying the model parameters based on physical data, two of the main hypotheses were tested: 1) elevation classes provide a natural scale for studying relationships between climate and orogeny; and

2) links between first order outlets and precipitation events are an important constraint on geomorphologic behavior. Although the first hypothesis was qualitatively demonstrated by the manner in which elevation classes denoted distinct precipitation regimes, the model results lent quantitative support by yielding effective uplift rates consistent with hypsometric curvature at the elevation class scale for each basin. The second hypothesis was substantiated by constraining the slope parameter to the maximum first order stream reliefs and lengths, and observing that the significance of the optimal dimensionless exponents of SPEL (4.4), chosen based on the slope constraint, matched the hypsometric analysis. Further, the effectiveness of the physical-statistical model as a means to study the feedback between local climate and orogeny, the third objective of this study, is supported by the significance of the optimum m and n values for each basin. The resulting values of these parameters matched the geomorphological characterizations established from the initial data analysis and found the same behavioral parings among the the basins.

6.1 Limiting Assumptions

The approach followed in this manuscript rests on a number of assumptions. First, we rely on the annual average of 14 years of precipitation data; thus, constraining our characterization of climate to a short, annual timescale. An alternative approach would be to use climate forcings outputted from climate models representative of millennial or million year timescales; however, climate model outputs will introduce their own uncertainties and errors into the analysis. However, a main goal of the analysis was to rely on both current climate and topographic organization as constraints to consider what these modern-day conditions imply about steady-state erosion and uplift processes. In this way, we demonstrate that climate has played a role in topographic evolution for each basin within the central Andes study area. The consistency between the estimated effective uplift rates and hypsometry and spatially

dependent tectonic forcing suggests that the approach of considering current climate is viable.

A second limiting factor in the analysis is the consideration of erosional processes as being solely dependent on precipitation amounts and impacts of regional ecology and vegetation on discharge and surface erosion were not taken into account. The specification of the physical-statistical model neglected erosion due to causes other than precipitation (e.g. glaciers and snow), as well as the impact that landslides and other highly destructive events may have on large-scale sediment redistribution. Here, discharge was strictly dependent on precipitation and basin size. Although the dimensionless SPEL parameters m and n account for regional erodibility behavior, we do not explicitly consider the effects of sediment removal due to extreme events or other possible contributors to the erosion process.

Finally, discharge is considered cumulative for regions that receive an influx of eroded sediments being redistributed from higher elevations. For each elevation class, the physical-statistical model assumes that all eroded sediments within that sub-region are removed. Thus, the uplift rates estimated act as upper bounds for each elevation class as we are neglecting incision power and aggradation. In fact, the basins with the highest erosion rates, the Huallaga and Ucayali, have segments of the first elevation class that are part of the foreland basin where eroded sediments from higher elevations collect and build-up over time. To investigate in part the effect that aggadation would have in these regions, we estimated uplift rates for the elevation classes of the Ucayali basin only considering discharge as the precipitation and area of each elevation class. The mean estimated uplift rate of each elevation class is consistent for the higher elevation classes where little aggradation occurs, but is much smaller for the lower elevation classes. Specifically, the average uplift rate estimated for the fifth elevation class is the same and for the lower elevation classes is approximately 2 mm/yr lower when compared to the uplift estimated with

cumulative discharge. Thus it appears that for this basin the effect of neglecting aggradation results in a difference of uplift rates on the order of 2 mm/yr.

6.2 Contributions

The major contributions of this work are the following. First, a model was developed that adequately captures geomorphic behavior, characterized through hypsometry, within and between basins. This model is also able to estimate uplift rates using SPEL as the physically-based process and returns reasonable estimates of regional uplift rates. We determined and tested a natural scale, the elevation class, which not only captures distinct topographic and climatic regimes, but also serves as a natural spatial scale to compare uplift rates and basin hypsometry. Finally, using the results of the physical-statistical model, a spatial trend in uplift behavior was observed that corresponded to the differential tectonic forcings experienced by the basins in the central Andes study region.

The task of quantitatively demonstrating the qualitative relationships between climate and orogeny observed in the literature and in Chapter 3 required the development of the physically-based statistical model. The direction followed in the present work was to estimate the magnitude of uplift at the elevation class scale in multiple basins based on current climate and topographic constraints. The approach of estimating uplift rates using SPEL within a Bayesian hierarchical model is the first of its kind. While the idea of incorporating a physical model within a Bayesian hierarchical framework is not new and has been explored in the environmental sciences (Berliner et al., 2008; Berliner, 2003; Berliner et al., 2000b; Campbell, 2004), the specific adaptation of the steady-state SPEL (4.4) into this framework has not been considered until now. Additionally, both the application of (4.4) at the watershed scale and its inversion to retrieve estimates of the U/K parameter regionally have not been considered. Although the focus of the present research was in the central

Andes, the simplicity of the physical-statistical model developed here easily allows for its application in other regions where the steady-state stream power erosion law is applicable. The completeness of the presentation of the derivation of the model could also serve as a template for building simple physically-based statistical model for other problems involving the estimation of parameters in empirical physical laws.

Previously measured uplift rates in the central Andes are typically between ~ 0 and 10 mm/yr. The results presented here, at the watershed-scale and without any specific geologic time dependence, for estimated uplift are determined using a common K-value and provide plausible estimates. The fact that this Bayesian statistical modeling approach yields physically reasonable estimates lends credence to the viability this novel method. Additionally, expected differences in uplift rates in relation to basin hypsometry were captured using this model. We have shown that the elevation classes proved an effective means to compare hypsometry and the effective uplift rates, which resulted in behavioral similarities. As the elevation classes also reflected distinct precipitation regimes within the basins, we were able to incorporate this link into the physical-statistical model to determine whether it operated as a first-order effect. The model then allowed for an exploration of geomorphology linked to a strong orographic precipitation.

6.3 Recommendations for Future Work

The application of the physical-statistical model developed here used a simple parameterization of precipitation and yet was able to capture the geomorphologic behavioral differences between and across basins in the central Andes. The demonstration of the effectiveness of this model under the simplest conditions for precipitation suggests more rigorous analysis could result from the use of a more sophisticated precipitation parameterization. One possibility includes incorporating the idea of a geomorpholoclimatic instantaneous unit hydrograph (GCIUH) to specify precipitation by

intensity, frequency, or duration, which has previously been incorporated with SPEL to test stream channel sensitivity to these rainfall characteristics (Wu et al., 2006). There is also potential to use the model with other configurations of SPEL that stress different assumptions for orogenic deformation, including self-similar wedges, threshold-limited, or sediment-flux transport iterations. What has been presented here is a flexible and interdiscplinary roadmap that may be adapted to a number of tectonic settings to better understand the relationship between climate and orogeny.

Appendix A

Derivations of Full Conditional Distributions of Model Parameters

Here we provide complete derivations of the full conditional distributions of each parameter in the physical-statistical model (see Chapter 4). The full conditional distributions are derived from (4.16) by considering only the terms that involve the parameter in question. Note that all parameters except for ϕ simplify into a standard-form distribution that is similar to the prior distributions chosen for them. This property is known as semi-conjugacy and allows for straightforward sampling via Gibbs. Gibbs sampling is a special case of Metropolis-Hastings algorithm described in Chapter 4, that allows for direct sampling from the full conditional distribution at each iteration. Since the full conditional distribution of ϕ does not result in a standard-form distribution, we must rely on Metropolis-Hastings. Each derivation shown below begins with only the terms in (4.16) that contain the parameter of interest.

Derivation of full conditional distribution for ϕ

$$p(\phi|-) \propto \exp\left[-\frac{1}{2\tau^2}\left(M - M_0\right)^2\right] \ \phi^{a-1}\exp\left[-b\phi\right] \tag{A.1}$$

$$= \phi^{a-1}\exp\left[-\frac{1}{2\tau^2}\left(M - \frac{1}{n}\phi + \frac{m}{n}D\right)^2 - b\phi\right] \tag{A.2}$$

$$= \phi^{a-1}\exp\left[-\frac{1}{2\tau^2}\left(M^2 + \frac{m^2}{n^2}D^2 + 2\frac{m}{n}DM - 2\frac{m}{n^2}D\phi - \frac{2}{n}M\phi + \frac{\phi^2}{n^2}\right) - b\phi\right] \tag{A.3}$$

$$\propto \phi^{a-1}\exp\left[-\frac{1}{2\tau^2}\left(\frac{\phi^2}{n^2} - 2\frac{m}{n^2}D\phi - \frac{2}{n}M\phi\right) - b\phi\right] \tag{A.4}$$

The full conditional distribution of ϕ does not simplify further into a standard form, and so we must use a Metropolis-Hastings sampling method to sample from this distribution.

Derivation of full conditional distribution for M

$$p(M|-) \propto \exp\left[-\frac{1}{2\sigma^2}\left(y - M\right)^2\right] \ \left(\frac{\mathbf{1}\left(M \in R\right)}{F(0) - F(\log\left(10^{-3}\right))}\right)\exp\left[-\frac{1}{2\tau^2}\left(M - M_0\right)^2\right] \tag{A.5}$$

$$= \left(\frac{\mathbf{1}\left(M \in R\right)}{F(0) - F(\log\left(10^{-3}\right))}\right)\exp\left[-\frac{1}{2}\left(\frac{1}{\sigma^2}\left(y^2 - 2My + M^2\right)\right.\right.$$
$$\left.\left. + \frac{1}{\tau^2}\left(M^2 - 2MM_0 + M_0^2\right)\right)\right] \tag{A.6}$$

$$\propto \left(\frac{\mathbf{1}\left(M \in R\right)}{F(0) - F(\log\left(10^{-3}\right))}\right)\exp\left[-\frac{1}{2}\left(M^2\left(\frac{1}{\sigma^2} + \frac{1}{\tau^2}\right) - 2M\left(\frac{y}{\sigma^2} + \frac{M_0}{\tau^2}\right)\right)\right] \tag{A.7}$$

Now let $\alpha = \frac{1}{\sigma^2} + \frac{1}{\tau^2}$ and $\beta = \frac{y}{\sigma^2} + \frac{M_0}{\tau^2}$.

$$= \left(\frac{\mathbf{1}\left(M \in R\right)}{F(0) - F(\log\left(10^{-3}\right))} \right) \exp\left[-\frac{1}{2}\left(\alpha M^2 - 2\beta M\right) \right] \times \exp\left[\frac{1}{2}\frac{\beta^2}{\alpha} - \frac{1}{2}\frac{\beta^2}{\alpha} \right] \quad \text{(A.8)}$$

$$= \left(\frac{\mathbf{1}\left(M \in R\right)}{F(0) - F(\log\left(10^{-3}\right))} \right) \exp\left[-\frac{\alpha}{2}\left(M^2 - 2\frac{\beta}{\alpha}M \right) + \frac{1}{2}\frac{\beta^2}{\alpha} - \frac{1}{2}\frac{\beta^2}{\alpha} \right] \quad \text{(A.9)}$$

$$= \left(\frac{\mathbf{1}\left(M \in R\right)}{F(0) - F(\log\left(10^{-3}\right))} \right) \exp\left[-\frac{\alpha}{2}\left(M^2 - 2\frac{\beta}{\alpha}M + \frac{\beta^2}{\alpha^2} \right) + \frac{1}{2}\frac{\beta^2}{\alpha^2} \right] \quad \text{(A.10)}$$

$$\propto \left(\frac{\mathbf{1}\left(M \in R\right)}{F(0) - F(\log\left(10^{-3}\right))} \right) \exp\left[-\frac{\alpha}{2}\left(M - \frac{\beta}{\alpha} \right)^2 \right] \quad \text{(A.11)}$$

$$\propto \mathrm{N}_R\left(\frac{\beta}{\alpha}, \frac{1}{\alpha} \right) \quad \text{or} \quad \mathrm{N}_R\left(\mu_n, \tau_n\right) \ , \quad R \in \left[\log\left(10^{-3}\right), 0\right] \quad \text{(A.12)}$$

where $\mu_n = \frac{y/\sigma^2 + M_0/\tau^2}{1/\sigma^2 + 1/\tau^2}$ and $\tau_n = \frac{1}{1/\sigma^2 + 1/\tau^2}$. We use Gibbs to sample M from a truncated normal distribution.

Derivation of full conditional distribution for $1/\sigma^2$

$$p(1/\sigma^2|-) \propto \left(\frac{1}{\sigma^2} \right)^{1/2} \exp\left[-\frac{1}{2\sigma^2}\left(y - M\right)^2 \right] \ \left(\frac{1}{\sigma^2} \right)^{c-1} \exp\left[-\frac{d}{\sigma^2} \right] \quad \text{(A.13)}$$

$$= \left(\frac{1}{\sigma^2} \right)^{c+1/2-1} \exp\left[-\frac{1}{\sigma^2}\left(\frac{\left(y - M\right)^2}{2} + d \right) \right] \quad \text{(A.14)}$$

$$\propto \mathrm{Ga}\left(c_n, d_n\right) \quad \text{(A.15)}$$

where $c_n = c + \frac{1}{2}$ and $d_n = \frac{(y-M)^2}{2} + d$. Since this distribution is semi-conjugate we can use Gibbs sampling.

Derivation of full conditional distribution for $1/\tau^2$

$$p(1/\tau^2|-) \propto \left(\frac{1}{\tau^2}\right)^{1/2} \exp\left[-\frac{1}{2\tau^2}\left(M - M_0\right)^2\right] \left(\frac{1}{\tau^2}\right)^{f-1} \exp\left[-\frac{g}{\tau^2}\right] \tag{A.16}$$

$$= \left(\frac{1}{\tau^2}\right)^{f+1/2-1} \exp\left[-\frac{1}{\tau^2}\left(\frac{\left(M - M_0\right)^2}{2} + g\right)\right] \tag{A.17}$$

$$\propto \mathrm{Ga}\left(f_n, g_n\right) \tag{A.18}$$

where $f_n = f + \frac{1}{2}$ and $g_n = \frac{\left(M-M_0\right)^2}{2} + g$. Again, we can take advantage of Gibbs sampling for this parameter.

Appendix B

Data Inputs for Physical-statistical Model

Careful consideration went into determining the values used as model inputs for the physical-statistical model. First, the values for slope in (4.6) were determined based on the relationship between first order outlets and precipitation events explored in Chapter 2. Due to similarities in how both physical metrics were distributed and the fact that the elevation class scale, also developed in Chapter 2, designated regions of qualitatively different behavior for the basins in the central Andes study region, we decide to use data from first order streams to specify the slope in the model. We believe that this choice not only incorporates our hypothesis that this apparent link between precipitation and outlets acts as a first-order effect on geomorphology, but also allows us to explore the whether the elevation class scale is a natural scale to characterize landscape evolution. As characteristic values for each elevation class, we use the maximum first order stream relief (Δz) and length (Δx).

The model input for discharge is also calculated at the elevation class scale to keep consistent with the slope model inputs. Since we are using digital elevation map (DEM) data to evaluate topography and distinguish elevation classes, we follow

standard procedures previously employed in the literature. When using DEM data to calculate discharge, Finlayson and Montgomery (2003) and Finlayson et al. (2002) suggest using a precipitation weighted cumulative area via

$$Q = \sum_{j=1}^{n} \alpha_j A_j P_j \tag{B.1}$$

where Q is the discharge, A is the area of a given grid cell, j, P is the precipitation amount within each cell, and α is a calibration coefficient in the instance rain gauge data is available (otherwise it is reasonable to set α=1). We similarly determine discharge for each elevation class, by approximating

$$Q_p = \sum_{k=p}^{m} \sum_{j=1}^{n} A_{k,j} P_{k,j} \tag{B.2}$$

where Q_p is the discharge for the elevation class p, m denotes the highest elevation class in the basin, n is the number of grid cells in the elevation class, and A and P are as before. For our purposes, we consider $\alpha = 1$. Thus, the discharge value used is cumulative for lower elevation classes. As stated in Chapter 2, we use both an adjusted and unadjusted mean annual precipitation (MAP) values computed from the TRMM 3B42 product and the Kospiñata rain gauge network in the Madre de Dios basin. Table B.1 lists all data values used for each of the six watersheds and their elevation classes.

Table B.1 Table of model inputs derived from data.

Basin	EC	Δz (m)	Δx (km)	Area (m^2)$\times 10^9$	MAP $\left(\frac{m}{yr}\right)$	adj. MAP $\left(\frac{m}{yr}\right)$
Marañón	1	1470	24.12	9.71	1.15	5.33
	2	1800	18.29	15.93	1.06	3.53
	3	1439	27.67	17.38	1.09	3.98
	4	1377	13.45	17.19	1.09	4.04
Huallaga	1	773	31.80	24.96	1.98	6.01
	2	927	22.79	8.38	2.03	6.49
	3	859	26.57	17.21	1.99	6.08
	4	927	20.92	10.45	1.97	5.92
	5	1037	27.20	27.54	1.72	3.65
Ucayali	1	1062	42.05	29.19	2.24	7.09
	2	1592	28.61	28.35	1.91	5.90
	3	1976	51.03	33.32	1.39	3.99
	4	2337	20.95	38.24	1.05	2.76
	5	1449	19.72	25.98	0.97	2.48
Madre de Dios	1	636	7.57	0.63	3.43	8.77
	2	499	13.06	1.48	2.95	6.77
	3	778	12.07	1.40	2.73	5.89
	4	1314	33.66	1.56	2.43	4.68
	5	247	10.48	1.96	2.06	3.17
Salar de Uyuni	1	618	32.05	11.12	0.34	–
	2	740	48.38	38.31	0.45	–
	3	809	69.64	21.53	0.48	–
	4	761	55.09	48.73	0.47	–
Beni	1	1718	19.28	1.07	1.55	6.13
	2	2358	41.18	5.29	1.47	5.62
	3	2320	19.19	9.46	1.47	5.62
	4	1677	19.55	11.62	1.32	4.74
	5	2097	19.37	2.06	1.09	3.31
	6	1894	15.57	5.45	1.01	2.83
	7	1721	13.93	9.17	0.90	2.14
	8	1047	14.46	2.38	0.82	1.69

Appendix C

Sample Autocorrelation Plots

When using Markov chain Monte Carlo (MCMC) sampling procedures, it is critical to check for autocorrelation in samples since the method is based on the current sample having some dependence on the value directly before it. However, what is not desired is for the current sample to have dependence on values prior to the most recently sampled value before it. Specifically, by testing for autocorrelation we are checking the speed of *mixing*, or rather measuring how quickly we move around the parameter space. To check for autocorrelation in the samples, the autocorrelation function (ACF) for each parameter is computed in Figure C.1. Along the x-axis, the lag gives an indication of the number of samples between iterations and the y-axis is the estimated correlation between these samples. The dashed lines mark the bounds of the 95% confidence region, and the solid lines that fall outside of this range denote statistical significance. There is high autocorrelation in the samples of ϕ and M, so we thin by taking 1 in every 4 samples. The ACF is computed once again for the thinned samples (see Figure C.2). We see that in the thinned plots, autocorrelation between samples decreases much more rapidly than in the samples without thinning.

These thinned samples are used in the posterior inferences summarized in Chapter 5 for ϕ and M.

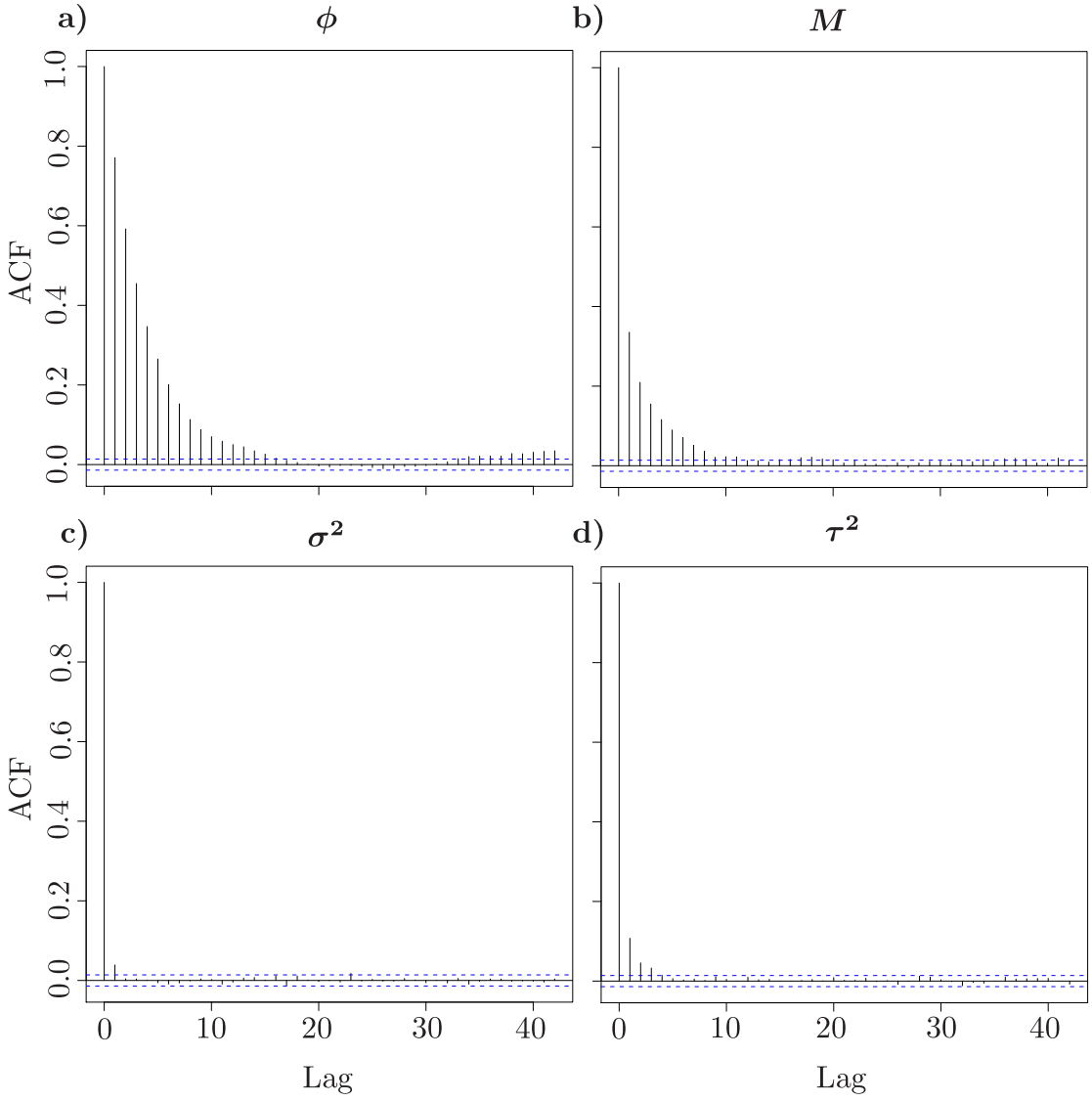

FIGURE C.1 Sample plots of autocorrelation for parameters of the physical-statistical model. a) ϕ. b) M. c) σ^2. d) τ^2.

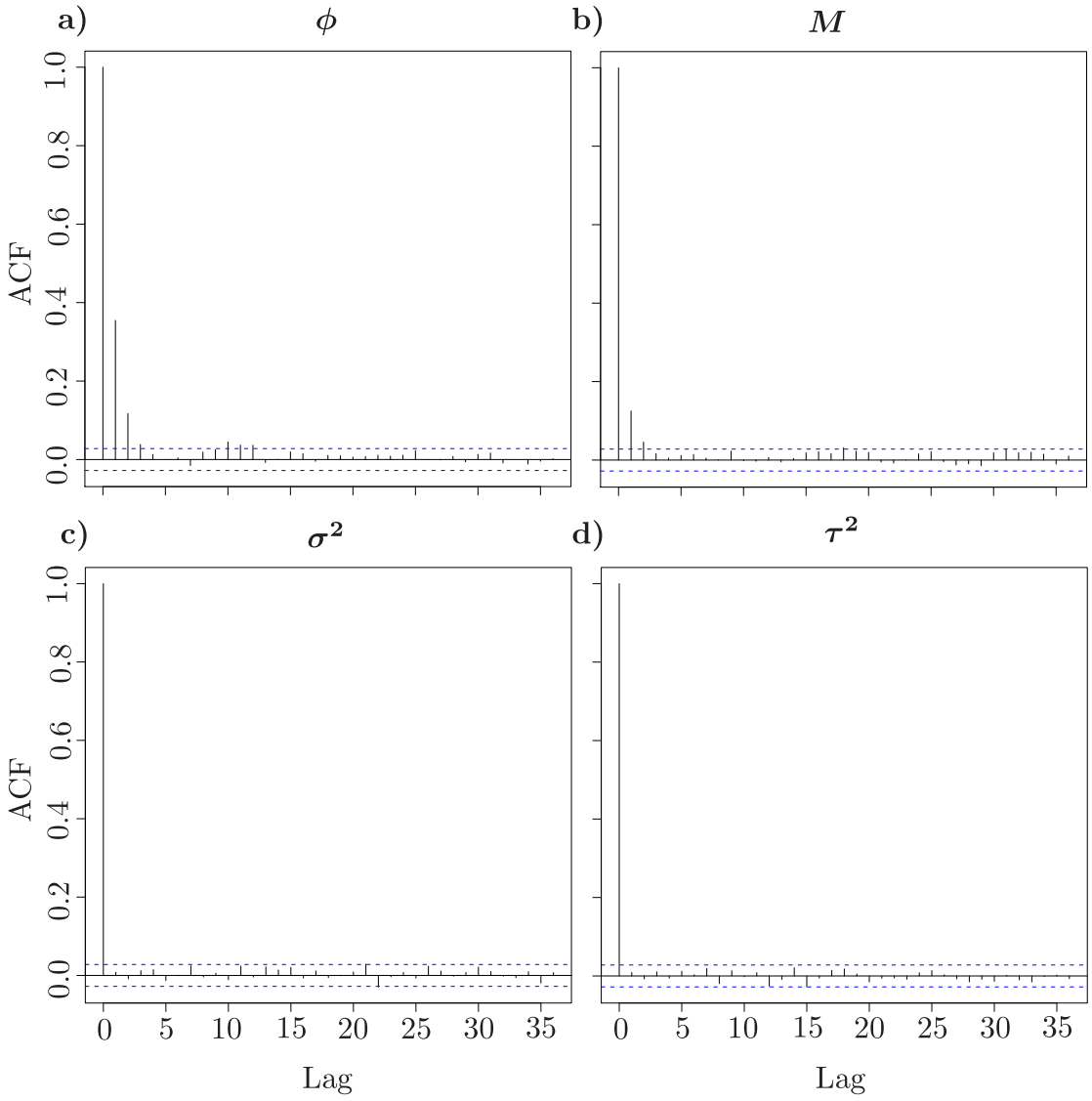

FIGURE C.2 Sample plots of autocorrelation after thinning every 1 in 4 samples for parameters of the physical-statistical model. a) ϕ. b) M. c) σ^2. d) τ^2.

Appendix D

Sample Trace Plots for Model Parameters

The purpose of this appendix is to demonstrate convergence in the Markov chain Monte Carlo (MCMC) sampling procedure employed in the physical-statistical model. The key observation necessary for convergence, also known as stationarity, is that samples taken from one part of the chain will have distributions similar to samples taken from other parts of the chain. For this reason, trace plots are shown for each of the parameters. To improve on autocorrelation in the samples, they are thinned by taking 1 in every 4. For further discussion of autocorrelation and thinning consult Appendix C. The trace plots in Figure D.1 have slow convergence, but show an improved convergence when samples are thinned in Figure D.2.

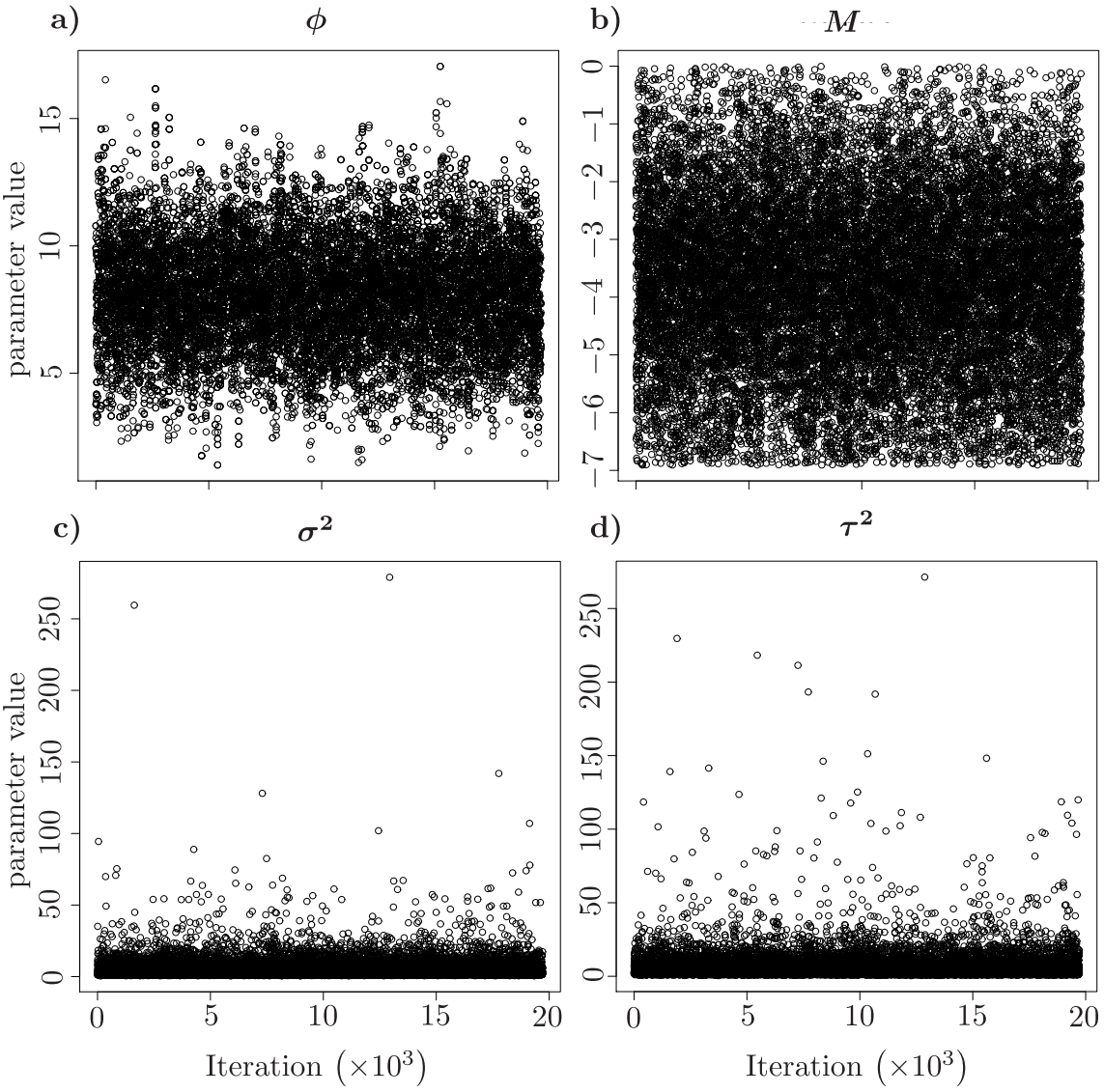

FIGURE D.1 Sample trace plots for the parameters of the physical statistical model. a) ϕ. b) M. c) σ^2. d) τ^2.

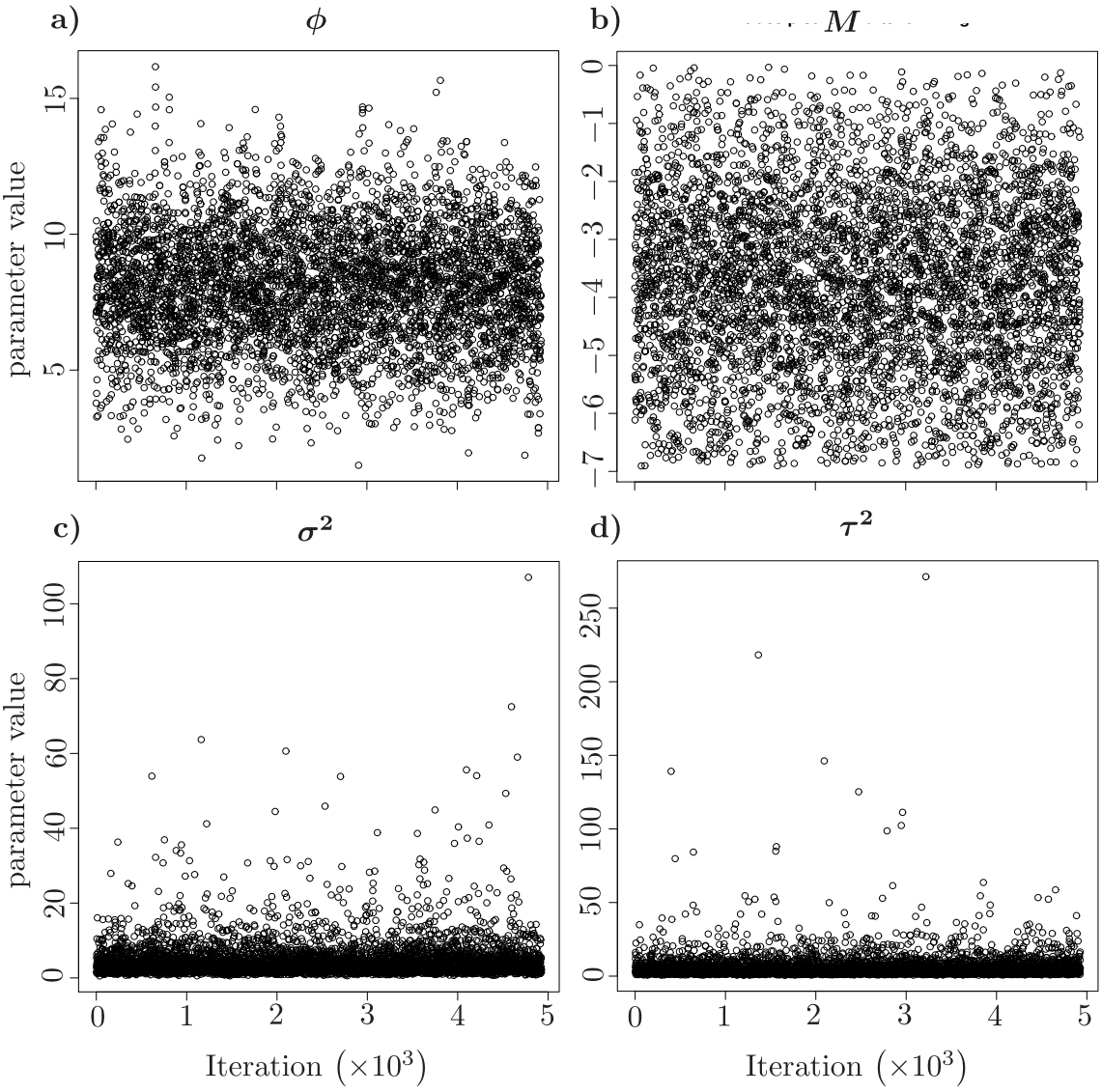

FIGURE D.2 Sample trace plots after thinning every 1 in 4 samples for the parameters of the physical statistical model. Notice the improved convergence for ϕ and M. a) ϕ. b) M. c) σ^2. d) τ^2.

Appendix E

Sample Posterior Distributions for Model Parameter ϕ

After thinning to improve mixing and ensure proper convergence in samples used for posterior inferences, we provide the posterior distributions for the unknown parameter ϕ calculated for each elevation class of the Marañón basin. The posterior distributions resemble closely those for the other watersheds as well. There is clear convergence towards a single mean in most distributions, however, we see that occasionally the posterior distributions result in some bi-modality. The two peaks are always very near to one another as seen in Figure E.1.

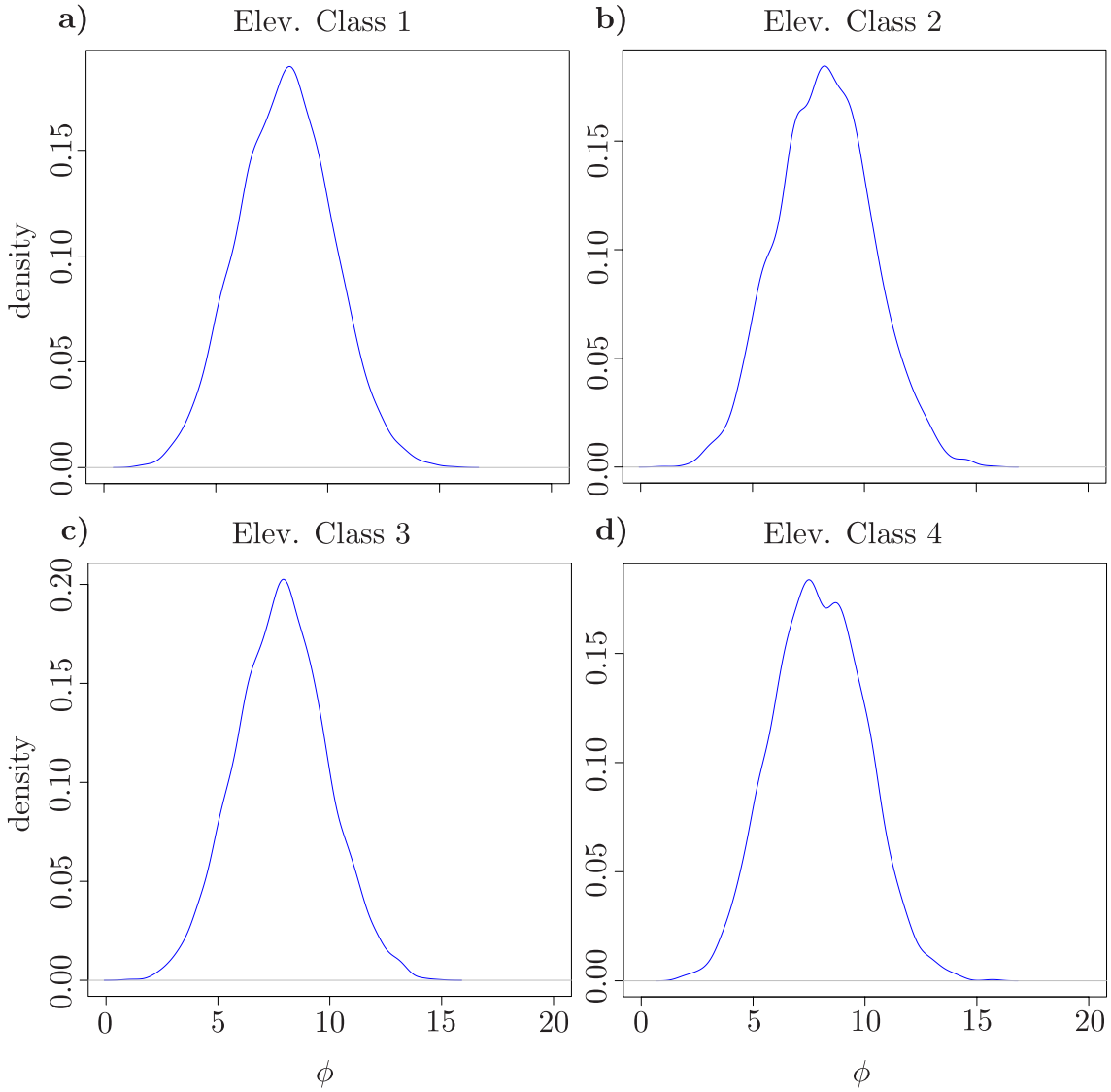

FIGURE E.1 Sample posterior distributions of ϕ for each elevation class of the Marañón basin. Here we demonstrate posterior convergence to a reasonable distribution. a) Elevation class 1. b) Elevation class 2. c) Elevation class 3. d) Elevation class 4.

Appendix F

Previously Measured Uplift Rates

A thorough review of the literature was conducted for previously measured uplift rates in the Andes mountains. An overview of each paper is provided in Table F.1 that includes the uplift or erosion rate measured, the estimated error for this measurement, and the methodology employed to obtain the measurement. Both uplift and erosion rates are considered, because under the steady-state assumption made in the present manuscript, these two values are equal.

Table F.1: Previously reported uplift rates for the Andes.

Reference	**Region**	**Uplift/Erosion (mm/y)**	**Error**	**Method**	**Notes**
Bookhagen and Strecker (2012)	NW Argentina, S. central Andes	$0.017 - 8.126$	± 2.236 $\frac{\text{mm}}{\text{yr}}$	cosmogenic nuclides	Erosion rates reported. The region considered falls outside the area of the present work's study region (farther south).
Fialko and Pearse (2012)	Bolivia, Altiplano-Puna	$0 - 10$	not reported	line-of-sight (LOS) velocity from ERS-2 and EnviSAT, 3D numerical models of a buoyant diapir	Uplift rates reported. The region considered falls outside the area of the present work's study region (farther south).
Gregory-Wodzicki (2000)	Eastern Cordillera	$0.2 - 0.3$	$1 - 1.5$ $\frac{\text{mm}}{\text{yr}}$	paleoelevation	Uplift rates reported for 10Ma to present.
Gregory-Wodzicki (2000)	Altiplano	$0.2 - 0.3$	$1 - 1.5$ $\frac{\text{mm}}{\text{yr}}$	paleoelevation	Uplift rates reported for 11Ma to present.
Lamb (2000)	Eastern Cordillera and Altiplano, Bolivian Andes	$0.01 - 2.5$	not reported	data-driven model that determines horizontal velocity field	Rock uplift rates based on material point estimates. Authors include figure that shows uplift increasing from west to east along transect at 20S.
Thouret et al. (2007)	Western Altiplano	$0.217 - 0.272$	not reported	paleosurfaces, ignimbrite chronostratigraphy	Surface uplift rate reported for 13-3.8Ma.

Continued on next page

Table F.1 – *Continued from previous page*

Reference	**Region**	**Uplift/Erosion (mm/y)**	**Error**	**Method**	**Notes**
Benjamin et al. (1987)	Zongo River, Bolivian Andes	0.7	$\sim$ 1km [*Gregory-Wodzicki*, 2000]	fission-track	Uplift rates reported. The authors find that when uplift rates are as a function of time, the resulting curve exhibits exponential growth. Thus, the authors conjecture that if this curve remains unbroken, uplift rates today may be significantly higher than the 0.7mm/yr reported for 3Ma. [*Gregory-Wodzicki*, 2000] refutes the conclusion of an exponential increase in uplift rates since 40Ma, claiming that the plot of 1/time vs time necessarily results in an exponential curve. She claims that the only conclusion supported is that denudation rates increased between 10-15Ma.
Garzione et al. (2008)	Central Andean Plateau	0.625	± 0.25 $\frac{\text{mm}}{\text{yr}}$	stable isotope paleoelevation	Surface uplift rate reported during Miocene ($\sim 10-6$Ma) period where rapid surface uplift is believed to take place.
Ghosh (2006)	Altiplano	1.03	± 0.12 $\frac{\text{mm}}{\text{yr}}$	clumped isotopes	Uplift rate reported for $\sim$ 10.3-6.7Ma.
Garzione et al. (2006)	Altiplano	$0.735-1.03$	not reported	clumped isotopes	Uplift rate reported during Miocene ($\sim$ 10.2-6.8Ma) period where rapid surface uplift is believed to take place.

Continued on next page

Table F.1 – *Continued from previous page*

Reference	**Region**	**Uplift/Erosion (mm/y)**	**Error**	**Method**	**Notes**
Schlunegger et al. (2006)	Lluta River Valley	0.1	$\sim$ 1km [*Gregory-Wodzicki*, 2000]	knickpoint analysis, valley morphology, fission-track dating	Surface uplift rate reported.
Barke and Lamb (2006)	Eastern Cordillera, Bolivian Andes	0.568	$\pm 0.232\ \frac{\text{mm}}{\text{yr}}$	along-stream river gradients, projecting paleo and modern river profiles w.r.t. paleosurfaces, knickpoint analysis	Rock uplift rates reported for 12-9Ma. Authors state that during this same period average erosion was $.077 \pm .03 \frac{\text{mm}}{\text{yr}}$. They give the formula: $U_s = U_r - E$.
Kennan (2000)	Eastern Cordillera, Bolivian Andes	0.2	$\sim$ 1km [*Gregory-Wodzicki*, 2000]	paleosurfaces and marine deposits	Surface uplift rate reported for c.a. 10Ma to present. Author claims fission-track dating only gives bulk erosion rates, not estimates of uplift. However, this data can be used to estimate a minimum age for surface uplift.
Crough (1983)	Cordillera Real, Bolivian Andes	$0.2 - 0.4$	$\sim$ 1km [*Gregory-Wodzicki*, 2000]	fission-track	Erosion rate reported for 12Ma to present.
Nelson (1982)	Cordillera Darwin, Chilean Andes	$0.05 - 0.07$	$\sim$ 1km [*Gregory-Wodzicki*, 2000]	fission-track	Surface uplift rate reported for 30Ma to present. The region considered falls outside the area of the present work's study region (farther south).

Continued on next page

Table F.1 – *Continued from previous page*

Reference	**Region**	**Uplift/Erosion (mm/y)**	**Error**	**Method**	**Notes**
Schildgen et al. (2009)	Western Andean Escarpment	$0.17 - 0.21$	$\sim$ 1km [*Gregory-Wodzicki*, 2000]	structural mapping, thermochronology, geochronology, fission-track	Surface uplift rate reported for 14Ma to present. The region considered is near to the Salar de Uyuni and Beni watersheds in the present work's study region.
Regard et al. (2010)	Central Andean coast, S. Peru to N. Chile	$0.09 - 0.64$	accuracies reported in paper by specific location	structural mapping, morphogenesis modeling	Uplift rates reported.
Lamb and Davis (2003)	Bolivian Andes at 20S	10	at least $\sim$ 1km	paleoaltimetry	Uplift rates reported for $14 - 6$Ma. Authors attribute recent rapid change in elevation to climate change (i.e. movement of Antarctic ice sheets).
Iaffaldano et al. (2006)	Region near Nazca-SA trench (20-30S, 71.5W)	0.3	$\sim$ 1km [*Gregory-Wodzicki*, 2000]	paleoaltimetry	Uplift rates reported for 3Ma to present. Authors find that fastest uplift rates occur during period of slow plate convergence.
Ehlers and Poulsen (2009)	Andean plateau	–	–	sensitivity studies with RCMs	Authors use a paleoclimate correction to the Andean plateau uplift history to demonstrate that constant slow growth over the last 25Ma is viable model. Show that temperature-dependent paleoaltimetry techniques will severely underestimate contemporaneous elevation when uncorrected for paleoclimate.

Continued on next page

Table F.1 – *Continued from previous page*

Reference	**Region**	**Uplift/Erosion (mm/y)**	**Error**	**Method**	**Notes**
Muñoz and Charrier (1996)	Chucal formation, N. Chile	0.038	± 0.002 $\frac{\text{mm}}{\text{yr}}$	paleoaltimetry	Uplift reported for 15-4.8Ma. Model used to deduce uplift assumed total exhumation over time period considered not isostatically compensated.
Ruiz et al. (2009)	Western Cordillera, SE Peru	$0.0125 - 0.025$	$\sim$ 1km [*Gregory-Wodzicki*, 2000]	fission-track	Surface uplift rate reported for 23-15Ma.
Norton and Schlunegger (2011)	Central Andes region	–	–	critical wedge deformation, stream power erosion law	The region considered is near to the Salar de Uyuni and Beni watersheds in the present work's study region. Authors show that due to orographic precipitation effect, erosion occurs faster on eastern slopes than western slopes. Also, eastern steams show positive feedback of rock uplift and orographic rainfall, where uplift for those in the west is due to tectonic forcing alone. Interesting, they use $m = 0.4$ and $n = 1$ in SPEL (transient and steady state). Seem to point to steady-state being appropriate for eastern basins. State that 10^6 years are time scale for channel response of orogen-sized rivers.

Bibliography

Aalto, R., Dunne, T., and Guyot, J. L. (2006), "Geomorphic controls on Andean denudation rates," *The Journal of geology*, 114, 85–99.

Allmaras, M., Bangerth, W., Linhart, J. M., Polanco, J., Wang, F., Wang, K., Webster, J., and Zedler, S. (2013), "Estimating Parameters in Physical Models through Bayesian Inversion: A Complete Example," *SIAM Review*, 55, 149–167.

Barke, R. and Lamb, S. (2006), "Late Cenozoic uplift of the Eastern Cordillera, Bolivian Andes," *Earth and Planetary Science Letters*, 249, 350–367.

Barros, A. (2013), "Orographic Precipitation, Freshwater Resources, and Climate Vulnerabilities in Mountainous Regions," in *Climate Vulnerability*, ed. Roger Pielke, pp. 57–78, Academic Press, Oxford.

Benjamin, M. T., Johnson, N. M., and Naeser, C. W. (1987), "Recent rapid uplift in the Bolivian Andes: Evidence from fission-track dating," *Geology*, 15, 680.

Berliner, L. M. (2003), "Physical-statistical modeling in geophysics," *Journal of Geophysical Research: Atmospheres*, 108.

Berliner, L. M., Levine, R. A., and Shea, D. J. (2000a), "Bayesian Climate Change Assessment," *Journal of Climate*, 13, 3805–3820.

Berliner, L. M., Wikle, C. K., and Cressie, N. (2000b), "Long-Lead Prediction of Pacific SSTs via Bayesian Dynamic Modeling," *Journal of Climate*, 13, 3953–3968.

Berliner, L. M., Milliff, R. F., and Wikle, C. K. (2003), "Bayesian hierarchical modeling of air-sea interaction," *Journal of Geophysical Research: Oceans*, 108.

Berliner, L. M., Jezek, K., Cressie, N., Kim, Y., Lam, C. Q., and Van Der Veen, C. J. (2008), "Modeling dynamic controls on ice streams: a Bayesian statistical approach," *Journal of Glaciology*, 54, 705–714.

Bookhagen, B. and Strecker, M. R. (2008), "Orographic barriers, high-resolution TRMM rainfall, and relief variations along the eastern Andes," *Geophysical Research Letters*, 35.

Bookhagen, B. and Strecker, M. R. (2012), "Spatiotemporal trends in erosion rates across a pronounced rainfall gradient: Examples from the southern Central Andes," *Earth and Planetary Science Letters*, 327-328, 97–110.

Brocklehurst, S. H. and Whipple, K. X. (2004), "Hypsometry of glaciated landscapes," *Earth Surface Processes and Landforms*, 29, 907–926.

Calvetti, D. and Somersalo, E. (2010), "Subjective Knowledge or Objective Belief? An Oblique Look to Bayesian Methods," in *Large-Scale Inverse Problems and Quantification of Uncertainty*, eds. L. Biegler, G. Biros, O. Ghattas, T. Heinkenschloss, D. Keyes, Banillick, Youssefrzouk, L. Tenorio, B. v. B. Waanders, and K. Willcox, p. 3370, John Wiley & Sons, Ltd.

Campbell, E. P. (2004), "An introduction to physical-statistical modelling using Bayesian methods," *CSIRO Mathematical and Information Sciences, Perth, Western Australia. Technical Report*, 49, 18.

Cohen, S., Willgoose, G., and Hancock, G. (2008), "A methodology for calculating the spatial distribution of the area-slope equation and the hypsometric integral within a catchment," *Journal of Geophysical Research*, 113.

Crough, S. T. (1983), "Apatite fission-track dating of erosion in the eastern Andes, Bolivia," *Earth and Planetary Science Letters*, 64, 396–397.

Efron, B. (2013), "Bayes' Theorem in the 21st Century," *Science*, 340, 1177–1178.

Ehlers, T. A. and Poulsen, C. J. (2009), "Influence of Andean uplift on climate and paleoaltimetry estimates," *Earth and Planetary Science Letters*, 281, 238–248.

Elsner, J. B. and Jagger, T. H. (2004), "A Hierarchical Bayesian Approach to Seasonal Hurricane Modeling," *Journal of Climate*, 17, 2813–2827.

Fialko, Y. and Pearse, J. (2012), "Sombrero Uplift Above the Altiplano-Puna Magma Body: Evidence of a Ballooning Mid-Crustal Diapir," *Science*, 338, 250–252.

Finlayson, D. P. and Montgomery, D. R. (2003), "Modeling large-scale fluvial erosion in geographic information systems," *Geomorphology*, 53, 147–164.

Finlayson, D. P., Montgomery, D. R., and Hallet, B. (2002), "Spatial coincidence of rapid inferred erosion with young metamorphic massifs in the Himalayas," *Geology*, 30, 219–222.

Garzione, C. N., Molnar, P., Libarkin, J. C., and MacFadden, B. J. (2006), "Rapid late Miocene rise of the Bolivian Altiplano: Evidence for removal of mantle lithosphere," *Earth and Planetary Science Letters*, 241, 543–556.

Garzione, C. N., Hoke, G. D., Libarkin, J. C., Withers, S., MacFadden, B., Eiler, J., Ghosh, P., and Mulch, A. (2008), "Rise of the Andes," *Science*, 320, 1304–1307.

Gasparini, N. M., Whipple, K. X., and Bras, R. L. (2007), "Predictions of steady state and transient landscape morphology using sediment-flux-dependent river incision models," *Journal of Geophysical Research: Earth Surface*, 112.

Ghosh, P. (2006), "Rapid Uplift of the Altiplano Revealed Through 13C-18O Bonds in Paleosol Carbonates," *Science*, 311, 511–515.

Giovannettone, J. P. and Barros, A. P. (2009), "Probing Regional Orographic Controls of Precipitation and Cloudiness in the Central Andes Using Satellite Data," *Journal of Hydrometeorology*, 10, 167–182.

Gregory-Wodzicki, K. M. (2000), "Uplift history of the Central and Northern Andes: a review," *Geological Society of America Bulletin*, 112, 1091–1105.

Hilley, G. E. and Strecker, M. R. (2004), "Steady state erosion of critical Coulomb wedges with applications to Taiwan and the Himalaya," *Journal of Geophysical Research*, 109.

Hilley, G. E., Strecker, M. R., and Ramos, V. A. (2004), "Growth and erosion of fold-and-thrust belts with an application to the Aconcagua fold-and-thrust belt, Argentina," *Journal of Geophysical Research*, 109.

Hodges, K. (2006), "Climate and the Evolution of Mountains," *Scientific American*, 295, 72–79.

Hoorn, C., Wesselingh, F. P., Steege, H. t., Bermudez, M. A., Mora, A., Sevink, J., Sanmartn, I., Sanchez-Meseguer, A., Anderson, C. L., Figueiredo, J. P., Jaramillo, C., Riff, D., Negri, F. R., Hooghiemstra, H., Lundberg, J., Stadler, T., Srkinen, T., and Antonelli, A. (2010), "Amazonia Through Time: Andean Uplift, Climate Change, Landscape Evolution, and Biodiversity," *Science*, 330, 927–931, PMID: 21071659.

Iaffaldano, G., Bunge, H.-P., and Dixon, T. H. (2006), "Feedback between mountain belt growth and plate convergence," *Geology*, 34, 893.

Kennan, L. (2000), "Large-scale geomorphology in the central Andes of Peru and Bolivia: Relation to tectonic, magmatic and climatic processes," in *Geomorphology and Global Tectonics (ed. M. Summerfield)*, pp. 167–192, Wiley, London.

Kirby, E., Whipple, K., and Harkins, N. (2008), "Topography reveals seismic hazard," *Nature Geoscience*, 1, 485–487.

Lamb, S. (2000), "Active deformation in the Bolivian Andes, South America," *Journal of Geophysical Research: Solid Earth*, 105, 25627–25653.

Lamb, S. and Davis, P. (2003), "Cenozoic climate change as a possible cause for the rise of the Andes," *Nature*, 425, 792–797.

McQuarrie, N., Ehlers, T. A., Barnes, J. B., and Meade, B. (2008), "Temporal variation in climate and tectonic coupling in the central Andes," *Geology*, 36, 999.

Moglen, G. E. and Bras, R. L. (1995), "The Effect of Spatial Heterogeneities on Geomorphic Expression in a Model of Basin Evolution," *Water Resources Research*, 31, 2613–2623.

Montgomery, D. R. (1994), "Valley incision and the uplift of mountain peaks," *Journal of Geophysical Research: Solid Earth*, 99, 1391313921.

Montgomery, D. R., Balco, G., and Willett, S. D. (2001), "Climate, tectonics, and the morphology of the Andes," *Geology*, 29, 579–582.

Muñoz, N. and Charrier, R. (1996), "Uplift of the western border of the Altiplano on a west-vergent thrust system, northern Chile," *Journal of South American Earth Sciences*, 9, 171–181.

Nelson, E. P. (1982), "Post-tectonic uplift of the Cordillera Darwin orogenic core complex: evidence from fission track geochronology and closing temperature–time relationships," *Journal of the Geological Society*, 139, 755–761.

Nesbitt, S. W., Zipser, E. J., and Cecil, D. J. (2000), "A Census of Precipitation Features in the Tropics Using TRMM: Radar, Ice Scattering, and Lightning Observations," *Journal of Climate*, 13, 4087–4106.

Norton, K. and Schlunegger, F. (2011), "Migrating deformation in the Central Andes from enhanced orographic rainfall," *Nature Communications*, 2, 584.

Pérez-Peña, J. V., Azañón, J. M., Booth-Rea, G., Azor, A., and Delgado, J. (2009), "Differentiating geology and tectonics using a spatial autocorrelation technique for the hypsometric integral," *Journal of Geophysical Research*, 114.

Regard, V., Saillard, M., Martinod, J., Audin, L., Carretier, S., Pedoja, K., Riquelme, R., Paredes, P., and Hrail, G. (2010), "Renewed uplift of the Central Andes Forearc revealed by coastal evolution during the Quaternary," *Earth and Planetary Science Letters*, 297, 199–210.

Rodríguez-Iturbe, I., González-Sanabria, M., and Bras, R. L. (1982), "A geomorphoclimatic theory of the instantaneous unit hydrograph," *Water Resources Research*, 18, 877–886.

Roe, G., Montgomery, D., and Hallet, B. (2003), "Orographic precipitation and the relief of mountain ranges," *Journal of Geophysical Research*, 108.

Roe, G. H., Montgomery, D. R., and Hallet, B. (2002), "Effects of orographic precipitation variations on the concavity of steady-state river profiles," *Geology*, 30, 143–146.

Ruiz, G. M. H., Carlotto, V., Heiningen, P. V. V., and Andriessen, P. a. M. (2009), "Steady-state exhumation pattern in the Central Andes SE Peru," *Geological Society, London, Special Publications*, 324, 307–316.

Schildgen, T. F., Hodges, K. V., Whipple, K. X., Pringle, M. S., van Soest, M., and Cornell, K. (2009), "Late Cenozoic structural and tectonic development of the western margin of the central Andean Plateau in southwest Peru," *Tectonics*, 28.

Schlunegger, F., Zeilinger, G., Kounov, A., Kober, F., and Husser, B. (2006), "Scale of relief growth in the forearc of the Andes of Northern Chile (Arica latitude, 18°S)," *Terra Nova*, 18, 217–223.

Sklar, L. and Dietrick, W. E. (1998), "River longitudinal profiles and bedrock incision models: stream power and the influence of sediment supply," in *Rivers Over Rock: Fluvial Processes in Bedrock Channels*, eds. K. J. Tinkler and E. E. Wohl, American Geophysical Union.

Snyder, N. P., Whipple, K. X., Tucker, G. E., and Merritts, D. J. (2000), "Landscape response to tectonic forcing: Digital elevation model analysis of stream profiles in the Mendocino triple junction region, northern California," *Geological Society of America Bulletin*, 112, 1250–1263.

Stock, J. D. and Montgomery, D. R. (1999), "Geologic constraints on bedrock river incision using the stream power law," *Journal of Geophysical Research: Solid Earth*, 104, 4983–4993.

Strahler, A. N. (1952), "Hypsometric (area-altitude) analysis of erosional topography," *Geological Society of America Bulletin*, 63, 1117–1142.

Strahler, A. N. (1957), "Quantitative analysis of watershed geomorphology," *Transactions, American Geophysical Union*, 38, 913.

Strecker, M., Alonso, R., Bookhagen, B., Carrapa, B., Hilley, G., Sobel, E., and Trauth, M. (2007), "Tectonics and Climate of the Southern Central Andes," *Annual Review of Earth and Planetary Sciences*, 35, 747–787.

Strecker, M. R., Alonso, R., Bookhagen, B., Carrapa, B., Coutand, I., Hain, M. P., Hilley, G. E., Mortimer, E., Schoenbohm, L., and Sobel, E. R. (2009), "Does the topographic distribution of the central Andean Puna Plateau result from climatic or geodynamic processes?" *Geology*, 37, 643–646.

Thouret, J.-C., Wrner, G., Gunnell, Y., Singer, B., Zhang, X., and Souriot, T. (2007), "Geochronologic and stratigraphic constraints on canyon incision and Miocene uplift of the Central Andes in Peru," *Earth and Planetary Science Letters*, 263, 151–166.

Tucker, G. E. and Bras, R. L. (2000), "A stochastic approach to modeling the role of rainfall variability in drainage basin evolution," *Water Resources Research*, 36, 1953–1964.

Tucker, G. E. and Whipple, K. X. (2002), "Topographic outcomes predicted by stream erosion models: Sensitivity analysis and intermodel comparison," *Journal of Geophysical Research*, 107.

Whipple, K. X. (2004), "Bedrock Rivers and the Geomorphology of Active Orogens," *Annual Review of Earth and Planetary Sciences*, 32, 151–185.

Whipple, K. X. and Meade, B. (2004), "Controls on the strength of coupling among climate, erosion, and deformation in two-sided, frictional orogenic wedges at steady state," *Journal of Geophysical Research*, 109.

Whipple, K. X. and Tucker, G. E. (1999), "Dynamics of the stream-power river incision model: Implications for height limits of mountain ranges, landscape response timescales, and research needs," *Journal of Geophysical Research: Solid Earth*, 104, 17661–17674.

Wikle, C. K. (2003), "Hierarchical Bayesian Models for Predicting the Spread of Ecological Processes," *Ecology*, 84, 1382–1394.

Willett, S. D. (1999), "Orogeny and orography: The effects of erosion on the structure of mountain belts," *Journal of Geophysical Research: Solid Earth*, 104, 28957–28981.

Willgoose, G. and Hancock, G. (1998), "Revisiting the hypsometric curve as an indicator of form and process in transportlimited catchment," *Earth Surface Processes and Landforms*, 23, 611–623.

Wu, S., Bras, R. L., and Barros, A. P. (2006), "Sensitivity of channel profiles to precipitation properties in mountain ranges," *Journal of Geophysical Research: Earth Surface*, 111.